Periodic Trends in Gas-phase Oxidation and Hydrogenation Reactions of Lanthanides and 5d Transition Metal Cations

P. B. Armentrout

315 S 1400 E Rm 2020, Department of Chemistry, University of Utah, Salt Lake City, UT 84112, USA

email: armentrout@chem.utah.edu; (801) 581-7885

Short title: Periodic trends in metal cation chemistry

Keywords: Bond energies, guided ion beam tandem mass spectrometry, lanthanides, thorium, transition metals

Biographical sketch

Peter B. Armentrout, Department of Chemistry, University of Utah, Utah, USA

Some 40 years ago, Professor Armentrout and his group developed the first guided ion beam tandem mass spectrometer to quantitatively examine the kinetic energy dependence of ion–molecule reactions. In the interim, he and his group have developed sophisticated tools for analyzing this dependence and thereby providing thermodynamic, kinetic, and dynamic information on a wide range of chemical species. Innovative use of a variety of ion sources has extended the applicability of these methods to a host of interesting inorganic and biological molecules. His group is well-known for providing quality thermodynamic information for species ranging from diatomic molecules, to atomic clusters, to solvated systems, and biopolymers. Professor Armentrout has been a faculty member in the Department of Chemistry at the University of Utah since 1987. He has been recognized by a number of awards and his research is documented in over 535 refereed articles and book chapters.

Acronyms:

AFRL – Air Force Research Laboratory

BDE – bond dissociation energy

CBS – complete basis set

CI – chemi-ionization

CID – collision-induced dissociation

DC/FT – dc discharge/flow tube

EI –electron ionization

GIBMS – guided ion beam tandem mass spectrometry

GVB – generalized valence bond

ICP – inductively coupled plasma

IE – ionization energy

LGS – Langevin-Gioumousis-Stevenson

QMF – quadrupole mass filter

MO – molecular orbital

MOSC – metal oxide space cloud

SI – surface ionization

SIFT – selected ion flow tube

TM^+ – transition metal cation

Table of Contents

I. INTRODUCTION

Of the many publications coming from the laboratory of Diethard K. Bohme, among the most valuable were the surveys of reactivity throughout the periodic table as studied using selected ion flow tube (SIFT) mass spectrometry. A convenient summary of this work can be found at http://www.yorku.ca/dkbohme/research/selection_table.html. It includes studies of the cations of main group, transition metal, and lanthanide elements with O_2 (Koyanagi & Bohme, 2001; Koyanagi et al., 2002), CO_2 (Cheng, Koyanagi & Bohme, 2006; Koyanagi & Bohme, 2006), OCS and CS_2 (Cheng, Koyanagi & Bohme, 2006; Cheng, Koyanagi & Bohme, 2006), NO (Blagojevic et al., 2005; Voislav Blagojevic, 2006), N_2O (Koyanagi & Bohme, 2001; Lavrov et al., 2004), NO_2 (Jarvis et al., 2010; Jarvis et al., 2013), CH_4 (Shayesteh et al., 2009), NH_3 (Koyanagi, Cheng & Bohme, 2010; Blagojevic et al., 2019; Blagojevic et al., 2019), D_2O (Cheng, Koyanagi & Bohme, 2006; Cheng, Koyanagi & Bohme, 2007), CH_3F (Koyanagi et al., 2005; Zhao, Koyanagi & Bohme, 2006), CH_3Cl (Zhao, Koyanagi & Bohme, 2005), SF_6 (Cheng & Bohme, 2006; Cheng, Shayesteh & Bohme, 2009), C_6H_6 (Voislav Blagojevic, 2015), C_6F_6 (Caraiman, Koyanagi & Bohme, 2004), and C_5H_5N (Blagojevic & Bohme, 2015). In all cases, quantitative rate constants at 295 K and 0.35 Torr of He were obtained for metal cations generated by an inductively coupled plasma (ICP). This source creates ions at a temperature characterized as 5500 K. It was believed that radiative relaxation and interactions with the flow gases would rapidly deplete most excited electronic states of the metal cations, although this is unknown. (Subsequent studies in our group verify that this is probably true for many of the metal cations, but not all. See discussion below.)

Although ion-molecule reactivity at room temperature provides a snapshot of the periodic trends and can potentially yield lower limits to metal ligand bond dissociation energies (BDEs), it cannot provide detailed thermodynamic information. In this review, we take a page from Bohme and examine the periodic trends in the reactions of metal cations using guided ion beam tandem mass spectrometry (GIBMS) (Armentrout, 1992; Armentrout, 2000; Armentrout, 2002). This experimental approach enables the reactions to be studied over a wide range of kinetic energies, essentially ranging from room temperature up to the equivalent of tens of thousands of degrees

(although with much narrower, well-defined energy distributions). This enables a direct visualization of the periodic trends in the thermodynamics and the reactivity, as well as serving as a mechanistic probe. For the purposes of the present review, we focus on oxidation (chiefly with O_2, CO, CO_2), carbidization (with CO), and hydrogenation (with H_2) reactions with cations of third-row (5d) transition metals, lanthanides, and the actinide thorium. For interested readers, a similar exploration of the periodic trends in the reactions of methane with the 5d transition metal cations (TM^+) has been published (Armentrout, 2017). Similar reviews of periodic trends in the first- (3d) and second-row (4d) TM^+ are also available (Elkind & Armentrout, 1986; Armentrout, 1990; Fisher et al., 1990; Armentrout & Botero, 1995; Armentrout & Kickel, 1996; Kretzschmar et al., 2001).

II. EXPERIMENTAL APPROACH

A. General

The experimental work reviewed here has been accomplished using GIBMS. Details of our instruments can be found elsewhere (Ervin & Armentrout, 1985; Loh et al., 1989; Muntean & Armentrout, 2001) and specifics of the individual experiments are provided in the original publications. Here we highlight the main attributes of our recent studies. The GIBMS instruments comprise five major parts: ion source, magnetic sector mass analyzer, ion-neutral interaction region, quadrupole mass filter (QMF), and ion detector. The ion sources and their attributes are described in the next section. Once the ions are formed, they are focused into the magnetic sector, which permits mass selection of the desired reactant ion with good transmission and approximately unit mass resolution. Ions are then focused into a radio frequency (rf) octopole ion beam guide pioneered by Gerlich (Teloy & Gerlich, 1974; Gerlich, 1992), which traps the ions in the radial direction without influencing their kinetic energy along the axis. The central dc voltage applied to the octopole can be varied over about four orders of magnitude and controls the kinetic energy of the ions in the laboratory frame. The octopole passes through a collision cell containing the reactant neutral. Because the octopole is longer than the reaction cell, ion-molecule collisions only occur

at well controlled kinetic energies, rather than in regions where ions are being focused and accelerated. In all of our studies, the pressure of the neutral reactant is kept low such that the probability of multiple ion-molecule collisions is small. To verify this, reactions are routinely conducted at several (generally three) neutral pressures and then the results are extrapolated to zero pressure, where rigorous single collision conditions apply. Ionic reactants and products then drift to the end of the octopole where they are focused into the QMF for separation. The QMF is operated under conditions where transmission is optimized so that it is generally believed that all ions are collected. Finally, the ion detector is a Daly detector (Daly, 1960) that utilizes a high voltage (~25 kV) primary dynode so that detection efficiency is near unity for all ions in our available mass range (up to ~250 Da and ~1100 Da on our two instruments).

Data collection involves acquisition of intensities of the reactant ion and all relevant product ions as a function of the laboratory voltage applied to the octopole. The absolute scale of this voltage is determined for each experiment by scanning the applied voltage through the zero of energy, nominally, the voltage of the ion source. The ion intensity of the reactant ions as a function of the applied voltage is differentiated and then fit to a Gaussian. This procedure enables determination of the center of the distribution (the zero of energy in the reaction zone) within 0.05 eV and the ion kinetic energy distribution width, which both vary from source to source. The raw ion intensities are then converted to absolute reaction cross sections by knowing the length of the interaction region and the density of the neutral gas, as described previously (Ervin & Armentrout, 1985). The absolute laboratory frame energy, E_{lab}, is also converted to the center-of-mass frame energy, E_{CM}, using $E_{CM} = E_{lab} \times m / (m + M)$, where m is the mass of the neutral reagent and M is the reactant ion mass. E_{CM} is the energy available to induce chemical reactions because the remaining energy ($E_{lab} - E_{CM}$) is tied up in linear momentum conservation.

The key capability of GIBMS is the ability to vary the kinetic energy of the ions over a wide range. This function is enabled by the trapping characteristics of the rf octopole because they permit the energy of the ions to be reduced close to zero without losing ions to radial diffusion. As shown in our initial work using this instrument, the reaction of Ar^+ with H_2, HD, and D_2 (Ervin &

Armentrout, 1985), the use of an octopole extends the lowest useful kinetic energy from about 1 eV to about 0.05 eV (eventually limited by the thermal motion of the reactant neutrals). This ability was verified by converting the cross sections to rate constants and reproducing thermal (300 K, 0.04 eV CM) measurements as well as drift tube measurements extending to 0.3 eV (CM) (Lindinger et al., 1977; Dotan & Lindinger, 1982). Interestingly, we also reproduced a single plasma jet result at 5000 K (Gaucherel & Rowe, 1977), although our results extended to the equivalent of over 30000 K.

B. Ion Sources

A variety of ion sources have been used in our laboratory to generate atomic metal ions over the years. Early results included those using surface ionization (SI) and electron ionization (EI) sources. One advantage of the SI source is that it can create a well-defined distribution of electronic states because the ions are emitted from a hot filament (variable over a range of about 1800 – 2500 K and measured by optical pyrometry) and presumed to have a distribution characterized by this temperature. This assumption has been verified by observing cross section magnitudes varying as predicted with the filament temperature (Aristov & Armentrout, 1986; Aristov & Armentrout, 1987; Sunderlin & Armentrout, 1988), by comparison with ion mobility data for Co^+ (van Koppen, Kemper & Bowers, 1992), and more recently by comparison with results for spin-orbit state-selected vanadium cations (Armentrout, Chang & Ng, 2020; Ng et al., 2021). EI sources produce an unknown distribution of electronic states, but because the electron energy can be varied over a very wide range, this source can produce highly excited electronic states. In GIBMS, these can generally be identified by examining shifts in the thresholds for endothermic reactions. Early studies also utilized a drift cell source in which ions generated by EI were thermalized by ~1000 collisions with Ar {Ervin, 1986 #736}. Studies with Fe^+ demonstrated that this source emitted ions with considerably less energy than the SI source (Elkind & Armentrout, 1986; Schultz & Armentrout, 1987; Schultz, Elkind & Armentrout, 1988; Loh et al., 1989). Comparisons between results obtained using the drift cell, SI, and EI sources enabled a determination of the reactivities of different electronic states for many first-row TM^+.

The ion source used for the metal ions that are the focus of the present review is a dc discharge/flow tube (DC/FT) source. Here, metal ions are created by sputtering the appropriate metal cathode using argon cations created in a dc (glow) discharge. This also creates an unknown distribution of electronic states, but the flow tube (1 m long in our source) thermalizes the population by collisions with the Ar and He carrier gasses in a 1:9 mixture. Comparison of SI and DC/FT results for endothermic reactions in a number of studies permitted us to determine that the distribution of electronic states usually emitted from the DC/FT source could be as low as 300 K or as high as 1100 K (Clemmer et al., 1994; Haynes & Armentrout, 1994; Chen, Elkind & Armentrout, 1995; Kickel & Armentrout, 1995; Kickel & Armentrout, 1995; Sievers et al., 1996). In general, we conservatively calculate the electronic energy distribution as 700 ± 400 K.

Importantly, we have observed cases where such thermalization of electronic states created in the DC/FT source is incomplete, e.g., Ag^+ (Chen & Armentrout, 1995), Au^+ (Li, Gorham & Armentrout, 2010), and Ir^+ (Kim & Armentrout, 2021). For Au^+, it was clear that the discharge conditions helped control the extent of excitation because additions of CH_4 in the discharge would systematically enhance the amount of excited ^3D ($5d^96s^1$) states. For both Ag^+ and Au^+, the lowest lying excited electronic states lie well above the $^1S(d^{10})$ ground states (≥4.86 and ≥1.86 eV, respectively), such that there are no curve crossings that are needed for efficient collisional quenching (Loh et al., 1989). In both cases, the excited states are easily removed by adding additional quenching gases: O_2 for Ag^+ and N_2O for Au^+. We have also found that Ir^+ ions having electronic energies > 1.39 eV are emitted from the DC/FT source, albeit with a population of only 0.01% (Kim & Armentrout, 2021). If the distribution is truly thermal, then this could indicate an electronic temperature of 1700 K. However, as for Ag^+ and Au^+, it seems more likely that some electronic state or states remain unquenched because they do not couple with surfaces evolving from lower energy states. One possibility for Ir^+ is the $^2P_0$ level of Ir^+, located at 1.390 eV (Kramida et al., 2012),which is the lowest energy J = 0 level, such that it may not couple well with lower energy levels, which all have J = 1 – 5.

One key aspect of the excited states of most TM^+ (as well as neutrals and anions) is that they

involve excitations between the valence s and d orbitals. The p orbitals are too high in energy to be populated appreciably. Because both s and d electrons have even parity, radiative (electromagnetic) coupling between them is parity forbidden and only magnetic dipole and electric quadrupole transitions are allowed. Therefore, these excited states tend to be long-lived (seconds), although many can be quenched by collisions (which generally requires a curve crossing) or removed by reactions. For the lanthanides and actinides, f orbitals are odd parity such that transitions to d orbitals are electric dipole allowed. This is less influential for the lanthanide cations because spin-orbit splitting generally spreads the energy level out substantially, such that fewer levels are occupied initially.

III. REACTIONS WITH O_2

A. 5d Transition Metal Cations

In 2002, Bohme and co-workers examined the reactions of 3d, 4d, and 5d TM^+ with O_2 in their ICP/SIFT apparatus (Koyanagi et al., 2002). They determined that the group 3 (Sc^+, Y^+, and La^+), group 4 (Ti^+, Zr^+, and Hf^+), group 5 (V^+, Nb^+, and Ta^+), and group 6 (Mo^+ and W^+) TM^+ all reacted exothermically via reaction 1 with efficiencies generally ranging from 42 – 82% (Mo^+ was only 13% efficient).

$$M^+ + O_2\,(^3\Sigma_g^-) \rightarrow MO^+ + O\,(^3P) \qquad (1)$$

Cr^+ and groups 7 – 11 all reacted either by O_2 addition or not at all (Mn^+ and Cd^+). These results are consistent with GIBMS studies of the 3d (Fisher et al., 1990) and 4d (Chen & Armentrout, 1995; Sievers, Chen & Armentrout, 1996) TM^+ (including the much lower reactivity of Mo^+). Comparable GIBMS results for the 5d TM^+, Hf^+ – Au^+, reacting with O_2 are collected in Figure 1 (Zhang & Armentrout, 2003; Hinton, Li & Armentrout, 2009; Li, Gorham & Armentrout, 2010; Armentrout, 2013; Armentrout & Li, 2013; Hinton, Citir & Armentrout, 2013). The results are consistent with those of Bohme in all cases. Hf^+, Ta^+, and W^+ react exothermically with no barrier evident. The efficiency of these reactions is close to unity for all three metals, as shown by the fact that they reproduce the Langevin-Gioumousis-Stevenson (LGS) collision cross section (Langevin,

1905; Gioumousis & Stevenson, 1958) over a wide range of energies. These efficiencies are somewhat higher than those obtained in the ICP/SIFT results (67, 82, and 79%, respectively), which could be a consequence of collisions with the He bath gas and/or the different distributions of electronic states. Similar differences have also been observed for lighter metals.

For the late 5d TM^+, Re^+ - Au^+, it is clear that they do not react efficiently at thermal energies (equivalent to the lowest energy point in Figure 1), in agreement with the work of Bohme. One can also rapidly ascertain that the thresholds for these endothermic reactions indicate that $D_0(M^+\text{-}O)$ come in the order Os > Re > Ir > Pt > Au. This order is quantified in Table 1, where values are obtained from analysis of each of the cross sections shown. For the early metal oxides, the bond energies are derived from reactions with CO (Hinton, Li & Armentrout, 2009) (discussed below) or from collision-induced dissociation (CID) reactions (Hinton et al., 2011). In the case of Au^+, two cross sections are shown in Figure 1, one (circles) corresponding to reactions of Au^+ (^1S, $5d^{10}$) and the other (triangles) to a reactant ion beam containing a small percentage of Au^+ ($^3D_{3,2}$, $5d^96s^1$), which have excitation energies of 1.86 (J = 3) and 2.19 (J = 2) eV (Kramida et al., 2012). It can be seen that the difference in the apparent thresholds between the two cross sections is about 2 eV.

For all metals in Figure 1 except Au^+, the cross sections decrease or decrease more rapidly above about 5 eV, as indicated by the arrow located at $D_0(O_2)$ = 5.117 eV (Ruscic & Bross, 2019). In all cases, this is because the MO^+ product ions of reaction 1 can have enough internal energy that the dissociation channel leading to M^+ + 2 O products becomes accessible. The exception of Au^+ indicates that this reaction occurs more impulsively such that the excess energy gets placed into relative translational energy of the products rather than internal energy.

The other notable aspect of the data in Figure 1 is that the cross section for OsO^+ exhibits two obvious features (Hinton, Citir & Armentrout, 2013). The same is true for ReO^+ (Armentrout, 2013), and, although not as evident, for IrO^+ as well (Armentrout & Li, 2013). In the latter system, this is mainly shown by the inflection in the data near 1.5 eV, and confirmed by modeling of this cross section. The possibility that electronic excited states of the metal cations were present in any

of these systems was evaluated thoroughly and demonstrated not to be the case. Assigning the higher energy features to formation of excited O (^{1}D) could also be ruled out as the energetics do not match. This left two plausible explanations. The first possibility is that the two features correspond to formation of different electronic states of the MO^+ product ions formed in a spin-forbidden process at low energies and a spin-conserving reaction at higher energies (thereby explaining the enhancement of the signal). This possibility had been postulated in a number of other previous studies that showed multiple cross section features {Stowe, 1990 #301;Schröder, 1997 #2300;Sievers, 1998 #598;Rue, 1999 #1466;Sievers, 1995 #590}, including lanthanides (Demireva, Kim & Armentrout, 2016; Armentrout et al., 2018; Demireva & Armentrout, 2018; Ghiassee, Kim & Armentrout, 2019; Ghiassee, Stevenson & Armentrout, 2021) and actinides (Armentrout & Peterson, 2020). The difficulty with this explanation for reaction 1 is that the triplet spin states of the O_2 ($^3\Sigma_g^-$) reactant and O (^{3}P) product mean that multiple spin states of M^+ couple with low-lying states of MO^+ such that all likely reactions are spin-allowed.

The second possible explanation is less intuitive and involves the fact that this triatomic system is constrained to a plane throughout the reaction. Thus, A′ and A″ surfaces do not mix efficiently and could lead to different reaction paths. Indeed, calculations of the potential energy surfaces for these reactions showed that surfaces of A′ and A″ symmetry are qualitatively different in the entrance channels for all three metals (Armentrout, 2013; Armentrout & Li, 2013; Hinton, Citir & Armentrout, 2013). For Re^+, no low-energy pathways are available along the A′ surfaces, whereas for Os^+ and Ir^+, A″ surfaces have barriers in the entrance channels. At higher kinetic energies, coupling of the A′ and A″ surfaces can occur by electronic-rotational (Coriolis) coupling, as observed for reactions of state-specific rare gas cations (Ar^+, Kr^+, and Xe^+) with H_2, D_2, and HD (Ervin & Armentrout, 1985; Ervin & Armentrout, 1986; Ervin & Armentrout, 1989). In this scenario, the low-energy behavior observed experimentally in Figure 1 would correspond to adiabatic reactions along the A″ surfaces of Re^+ and the A′ surfaces of Os^+ and Ir^+. Then, the high-energy feature observed experimentally would be associated with reactions along the surfaces having the alternate symmetry with possible contributions from Coriolis coupling between the two.

To test these explanations, GIBMS studies of related oxidation processes have also been studied, in particular, reactions of Re^+, Os^+, and Ir^+ with CO (Kim, Cox & Armentrout, 2016) and SO_2 (Kim & Armentrout, 2020; Kim, Cox & Armentrout, 2020; Kim & Armentrout, 2021). The CO reactions retain the triatomic character of the O_2 reactions but now the CO reactant has singlet spin, which restricts the number of spin-allowed pathways. As discussed further below, the thresholds for these reactions provide thermochemistry in good agreement with that obtained from the O_2 reactions, even in a case like Re^+ where the formation of ground state products is formally spin-forbidden: $Re^+ (^7S) + CO (^1\Sigma^+) \rightarrow ReO^+ (^3\Delta) + C (^3P)$. Only a single cross section feature was observed in all three reactions, but because the CO bond is very strong, 11.111 eV (Ruscic & Bross, 2019), the endothermicities in all three cases exceed energies where the Coriolis coupling is likely. A better test of the spin-conservation restriction would be the oxidation reaction with CO_2 because now both the neutral reactant, CO_2 ($^1\Sigma_g^+$), and product, CO ($^1\Sigma^+$), have singlet spin. At the time of this writing, studies of this reaction for Re^+, Os^+, and Ir^+ are ongoing.

With regard to the second explanation, the SO_2 reactions were more insightful, in part because the thermochemistry, $D_0(OS\text{-}O) = 5.66$ eV (Johnson III, 2018), is similar to that for O_2, $D_0 = 5.117$ eV. Thresholds for the formation of MO^+ using the SO_2 reactant gave thermochemistry that was in excellent agreement with that found for the O_2 reactions. Further, only a single cross section feature for formation of MO^+ was observed for all three metal cations. Because these are four-atom systems, the MSO_2^+ reactions are no longer constrained to have planar symmetry. Thus, these results are consistent with the second explanation above for the dual features in the O_2 reactions.

B. Lanthanide Cations

GIBMS has been used to study the reactions of O_2 with four lanthanide cations: Pr^+ (Ghiassee, Stevenson & Armentrout, 2021), Nd^+ (Ghiassee, Kim & Armentrout, 2019), Sm^+ (Cox et al., 2015), and Gd^+ (Demireva, Kim & Armentrout, 2016; Demireva & Armentrout, 2017). As expected from their placement in the periodic table, all four metal cations react with O_2 similarly to the early transition metals shown in Figure 1, i.e., they react efficiently in exothermic and

barrierless processes, Figure 2. In our studies, the efficiencies of these four reactions at thermal energies were 1.75 ± 0.35, 0.93 ± 0.2, 1.0 ± 0.2, and 1.0 ± 0.2, respectively. The unusually large result for Pr^+ was double checked and two additional reactions ($Ar^+ + D_2$ and $Sm^+ + O_2$) were reproduced to try to ensure that instrumental issues were not responsible. Cross sections larger than the LGS collision limit have been observed for comparable species, Zr^+ and Nb^+ (Sievers, Chen & Armentrout, 1996). One explanation for this unusual result was explored in that study and involves coupling of the surfaces evolving from the $M^+ + O_2$ reactants with those associated with the $M^{2+} + O_2^-$ asymptote. The resulting long-range Coulomb attraction can lead to an enhancement of the collision limit. In this regard, the result is analogous to the harpooning mechanism observed in neutral reactions (Wiskerke et al., 2000).

For the four lanthanides, the GIBMS efficiencies are larger than the those measured in the ICP/SIFT apparatus: 0.75 ± 0.23, 0.57 ± 0.17, 0.48 ± 0.14, and 0.86 ± 0.26, respectively (Koyanagi & Bohme, 2001). In conjunction with the GIBMS study for Sm^+, additional flow tube studies on this reaction were also conducted and reproduced the ICP/SIFT efficiency, measuring 0.49 ± 0.15 (Cox et al., 2015). Interestingly, this reaction has been revisited using the same apparatus with improved mass resolution where it was discovered that the earlier work had a contribution from SmH^+, which reacts inefficiently with O_2. The revised flow tube rate constants put the reaction efficiencies at 300 K as 0.65 ± 0.20 for Sm^+ and 0.75 ± 0.23 for Nd^+, within experimental uncertainty of the GIBMS results. Remaining differences may still be attributed to variations in the electronic levels populated and the high-pressure flow tube gases versus single collision conditions in the GIBMS experiments.

Figure 2 also illustrates another aspect of exothermic ion-molecule reactions when studied as a function of energy. It can be seen that the cross sections for Nd^+, Sm^+, and Gd^+ follow the LGS prediction with fidelity at the lowest energies, but then deviate to smaller values starting at different energies: ~0.3 eV for Sm^+, around 1 eV for Nd^+, and slightly higher for Gd^+. Likewise, the Pr^+ cross section declines approximately in parallel to σ_{LGS} before declining more abruptly near 1.5 eV. These deviations from LGS behavior occur because the rate-limiting step in the

reaction moves from the centrifugal barrier in the entrance channel (which defines the LGS collision limit) to the centrifugal barrier in the exit channel as the kinetic energy increases. This concept was first outlined in a study of the $O^+ + H_2$, HD, and D_2 reactions (Burley, Ervin & Armentrout, 1987) and involves conservation of the orbital angular momentum of the collision. In reaction 1, the reduced mass of the products is about half that of the reactants, such that the centrifugal barrier in the product channel increases more rapidly with energy than that in the reactant channel. (The fact that the polarizability of the O product is about half that of the O_2 reactant also plays a role in how attractive the potential is at long range.) At sufficiently high energies, the barrier in the product channel exceeds that in the reactant channel, such that not all close collisions can conserve angular momentum when making products and hence are forced to return to reactants. The energy where this crossover occurs depends on the exothermicity of reaction 1, i.e., a larger exothermicity requires a larger angular momentum (and collision energy) for the two barriers to match. Thus, the deviation between the experimental and LGS cross section will occur at lower energies for small exothermicities and this energy will increase with the exothermicity of the reaction. Examination of Figure 2 therefore suggests that the Sm^+ reaction is the least exothermic, followed by Nd^+, Gd^+, and Pr^+ being roughly similar. As detailed below in the thermochemistry section, this trend follows the BDEs of these MO^+ products.

At still higher energies, the MO^+ cross sections for all four lanthanides level out and then decline rapidly again at the highest energies shown. The leveling may indicate that the reaction cross sections are now limited by hard sphere limits. The rapid declines at high energies are associated with the dissociation of the MO^+ product. As noted above for the AuO^+ cross section, the observation that these declines occur at higher energies than $D_0(O_2)$ indicates more impulsive collision processes. Indeed, a spectator stripping model, in which the metal cation interacts with only one oxygen atom and the other oxygen serves as a spectator (Henglein, 1966; Burley, Ervin & Armentrout, 1987), roughly predicts the onsets of the dissociation.

C. Thorium Cation

GIBMS has also been used to study the reaction of thorium cation with O_2 (Cox et al.,

2016). As for the lanthanides, Th^+ reacts efficiently in an exothermic and barrierless process with an efficiency of 1.21 ± 0.24 at thermal energies, Figure 2. This result agrees well with Fourier transform ion cyclotron resonance (FT-ICR) mass spectrometry studies, which obtain thermal rate constants having efficiencies of 1.12 ± 0.22 (Cornehl et al., 1997) and 0.86 ± 0.43 (Santos et al., 2002). At energies above thermal, the $Th^+ + O_2$ reaction exhibited a cross section exceeding the LGS limit. As for the Pr^+ case discussed above, the possibility of a crossing with the $Th^{2+} + O_2^-$ asymptote was suggested. Compared to the four lanthanides, the deviation from the low-energy behavior occurs at higher energies than for Pr^+, consistent with reaction 1 for Th^+ having the highest exothermicity among the metals in Figure 2 (see below).

IV. REACTIONS WITH CO

A. 5d Transition Metal Cations

Bohme has not systematically studied reactions of TM^+ with CO largely because the strong CO bond precludes the observation of activation processes at thermal energies. Likewise, GIBMS studies of reactions with CO have not been conducted for many metal cations because these reactions were not needed to obtain good metal oxide thermochemistry. One exception is Cu^+, where studies of both the ground state ^1S and excited state ^3D were conducted (Rodgers, Walker & Armentrout, 1999). In contrast, for the early metal cations having strong metal oxide bonds, the strong CO bond makes the oxidation reaction endothermic. Hence, we have studied the CO reactions with the early 4d TM^+: Y^+, Zr^+, Nb^+, and Mo^+ (Sievers, Chen & Armentrout, 1996). For the 5d TM^+, reactions with CO have been conducted for Hf^+, Ta^+, W^+ (Hinton, Li & Armentrout, 2009), Re^+, Os^+, Ir^+ (Kim, Cox & Armentrout, 2016), and Pt^+ (Zhang & Armentrout, 2003). These results are collected in Figure 3. In all cases, two reactions are observed and yield the metal oxide and metal carbide cations, reactions 2 and 3.

$$M^+ + CO\ (^1\Sigma^+) \rightarrow MO^+ + C\ (^3P) \quad (2)$$

$$\rightarrow MC^+ + O\ (^3P) \quad (3)$$

Figure 3a shows that the cross sections for reaction 2 all increase rapidly from threshold and

eventually peak at $D_0(CO)$ = 11.111 eV before declining because the MO^+ product can dissociate at higher energies. The relative thresholds inversely track the MO^+ BDEs, such that the bonds come in the order $TaO^+ > HfO^+ > WO^+ > OsO^+ \sim ReO^+ > IrO^+ > PtO^+$. This progression is discussed further below in the thermochemistry section.

Figure 3b shows similar results for reactions with CO yielding the metal carbide cation. Again, the cross sections generally reach a maximum at $D_0(CO)$. Pt^+ is an exception because reaction 3 competes with reaction 2, such that the total cross section (shown by the line in Figure 3b) does peak at 11.111 eV. As for reactions 2, the thresholds of reactions 3 are inversely related to the bond strengths, indicating an order of $IrC^+ \sim OsC^+ > PtC^+ > ReC^+ > WC^+ > TaC^+ > HfC^+$, close to the inverse of the oxide BDEs. This is rationalized in the thermochemistry section below.

B. Lanthanide and Thorium Cations

The cross sections for reactions of CO with the lanthanide cations: Pr^+ (Ghiassee, Stevenson & Armentrout, 2021), Nd^+ (Ghiassee, Kim & Armentrout, 2019), Sm^+ (Cox et al., 2015), and Gd^+ (Demireva, Kim & Armentrout, 2016), and Th^+ (Cox et al., 2016) are shown in Figure 4. The behavior is comparable to that of the early 5d TM^+. Again, the thresholds inversely track the BDEs, with $ThO^+ > PrO^+ \sim GdO^+ > NdO^+ > SmO^+$ and $ThC^+ > GdC^+ \sim PrC^+ > NdC^+ > SmC^+$.

V. REACTIONS WITH CO_2

In 2006, Bohme and coworkers examined the reactions of carbon dioxide with atomic cations of main group, transition metals (except Tc^+)(Koyanagi & Bohme, 2006), and lanthanides (except for Pm^+)(Cheng, Koyanagi & Bohme, 2006). Among the main group and transition metal elements, only Sc^+, Ti^+, Y^+, Zr^+, La^+, Hf^+, Ta^+, and W^+ react to transfer an oxygen atom yielding MO^+. All other elemental ions examined simply cluster with CO_2 in three-body reactions. Efficiencies in the oxidation reactions vary wildly from Y^+ (80%) and La^+ (61%) to Ti^+ (5%). Likewise, for the lanthanides, about half react by oxygen atom transfer (La^+, Ce^+, Pr^+, Nd^+, Gd^+, Tb^+, and Lu^+) with efficiencies of 64%, 66%, 23%, 5%, 50%, 6%, and 5%, respectively. All other

lanthanide cations simply cluster.

GIBMS studies of these reactions are more limited because they often do not provide useful thermodynamic information. Early studies included those involving Al^+ (Clemmer, Weber & Armentrout, 1992), V^+ (Sievers & Armentrout, 1995), Cu^+ (Rodgers, Walker & Armentrout, 1999), Y^+ (Sievers & Armentrout, 1999), Zr^+ (Sievers & Armentrout, 1999), Nb^+ {Sievers, 1998 #598}, and Mo^+ {Sievers, 1998 #595}. The results at low energies are in accord with the results of Bohme and coworkers, but at higher energies, there are clear new features in the cross sections that have been interpreted as the production of excited states of the MO^+ products. In all cases but Al^+, endothermic reactions forming $MCO^+ + O$ are also observed and, in most cases, formation of $MO_2^+ + C$ (not Al^+, Cu^+, or Y^+) is also observed.

These types of behaviors are also illustrated in more recent GIBMS work on reactions of CO_2 with Pr^+ (Ghiassee, Stevenson & Armentrout, 2021), Nd^+ (Ghiassee, Kim & Armentrout, 2019), Sm^+ (Armentrout & Cox, 2017), Gd^+ (Demireva & Armentrout, 2018), and Pt^+ (Zhang & Armentrout, 2003). Results from these processes are shown in Figure 5, which does not include results for the MO_2^+ product. Again, the results are qualitatively in agreement with those of Bohme and coworkers: oxidation of Pr^+, Nd^+, and Gd^+ occur at thermal energies, whereas those for Sm^+ and Pt^+ do not. For the three exothermic reactions, the efficiencies are 25%, 9%, and 70%, within experimental uncertainties of the ICP-MS results. At the lowest collision energies, the cross sections for these three processes decline more rapidly than predicted by the LGS collision limit and then increase starting near 1 eV or so, nearly reaching the predicted LGS limit at higher energies (although at these energies, the collision cross section is probably better described by a hard-sphere limit). Oddly, the oxidation reaction with Sm^+ is actually exothermic, but in contrast to most ion-molecule reactions, it clearly shows a barrier (measured as 1.77 ± 0.11 eV). In contrast, the reaction of Pt^+ with CO_2 begins at its thermodynamic threshold. Here, the shape of the $PtO^+ +$ CO cross section is clearly affected by the competing $PtCO^+ + O$ channel, such that the sum of the two cross sections (line in Figure 5) behaves smoothly. For the other metals shown here, the MCO^+ cross sections are much too small to show any effect on the MO^+ cross sections. In all cases, the

MCO^+ cross sections begin to decline near $D_0(OC\text{-}O)$ = 5.453 eV (Ruscic & Bross, 2019), and more subtle declines also occur starting near this energy for the MO^+ cross sections. The reason the MCO^+ cross sections decline much more rapidly than the MO^+ cross sections can be traced to the fact that the CO product formed with MO^+ can carry away more energy (in rotations, translations, and vibrations) than the lighter O product formed with MCO^+.

The MO^+ cross sections are sensitive to electronic state because the spin states of the neutral reactants and products for reactions 4 are both singlets, and therefore, spin conservation demands that the spin states of MO^+ must be the same as those for the M^+ reactant.

$$M^+ + CO_2\ (^1\Sigma_g^+) \rightarrow MO^+ + CO\ (^1\Sigma^+) \qquad (4)$$

This situation is rarely the case because formation of a strong bond requires coupling of the two valence electrons on oxygen with those on the metal. For example, the ground states in the reactions shown in Figure 5 are Pr^+ (^{5}I) and PrO^+ (^{3}H), Nd^+ (^{6}I) and NdO^+ (^{4}H), Sm^+ (^{8}F) and SmO^+ ($^6\Delta$), Gd^+ (^{10}D) and GdO^+ ($^6\Sigma^-$), and Pt^+ (^{2}D) and PtO^+ ($^4\Sigma^-$). Although reactions for most heavy metal systems are not truly spin-forbidden (i.e., not occurring) because of spin-orbit coupling, reactions that do not conserve spin can be inefficient because surfaces of different spin need to couple to one another. This partially explains the large variations in efficiencies observed in the studies of Bohme and coworkers as well as in the GIBMS studies, as they rely on where the curves between potential energy surfaces of the two spin states intersect. The fact that the exothermic processes decline more rapidly than predicted by the LGS cross section, e.g., as in Figure 5, is consistent with the energy dependence expected for spin-forbidden reactions (Rue et al., 1999). Because the exothermic spin-forbidden processes are inhibited, spin-allowed reactions, which can be more efficient because no curve crossings are required, can then be observed at higher energies. For example, calculations at multiple levels of theory indicate that the lowest energy MO^+ states having the same spin as the M^+ reactant should have thresholds of 0.5 – 1.5 eV for Pr^+ (Ghiassee, Stevenson & Armentrout, 2021), 0.6 – 1.8 eV for Nd^+ (Ghiassee, Kim & Armentrout, 2019), and 0.6 – 1.1 eV for Gd^+ (Demireva & Armentrout, 2018), in agreement with the measured onsets for the observed endothermic features of 0.69 ± 0.12, 0.85 ± 0.12, and 1.01 ± 0.12 eV, respectively.

The case of the Sm^+ reaction is more interesting. Here, GIBMS studies are able to take advantage of the fact that the reverse of reaction 4 can be studied (and has been in all of the systems mentioned here except Al^+ and Cu^+). When reaction 4 (ignoring spin) is exothermic, the reverse process must be endothermic, and indeed, the reverse of reaction 4 can be analyzed to yield an endothermicity that provides an independent measure of the MO^+ bond energy. In the case of Sm^+, the $SmO^+ + CO \rightarrow Sm^+ + CO_2$ reaction was also observed to be endothermic, with a threshold of 2.04 ± 0.13 eV. The difference between the thresholds for the forward (1.77 eV) and reverse (2.04 eV) reactions is equivalent to the exothermicity of reaction 4 for Sm^+, 0.27 ± 0.07 eV (Armentrout & Cox, 2017). Here, theoretical calculations indicate that the barrier observed for reaction 4 with Sm^+ corresponds to the crossing point between the octet spin surface evolving from reactants to the sextet spin surface leading to products, calculated as 1.5 eV. Theory also suggests contributions from the spin-allowed formation of SmO^+ ($^8\Sigma^-$) may start at 2.3 – 2.8 eV. For Sm^+, the crossing point between surfaces of different spin is relatively high in energy because the diabatic surface leading to products starts from an excited Sm^+ ($4f^5 5d^2$) configuration, which lies 2.35 eV above the Sm^+ (^8F, $4f^6 6s^1$) ground state. As discussed further below, the promotion energies to M^+ ($5d^2$) states of the other lanthanide cations in Figure 5 are much lower, which means the exothermicities of the reactions are larger and the analogous crossing points between surfaces occur below the energy of the reactants.

VI. REACTIONS WITH H_2

Hydrogenation of metal cations is another system not explored by Bohme because the activation reaction 5 is endothermic.

$$M^+ + H_2 \rightarrow MH^+ + H \qquad (5)$$

Importantly, the activation of the single covalent bond in H_2 is the simplest system for examining bond activation processes by metals, such that GIBMS studies have been comprehensive. This work includes the 3d (Elkind & Armentrout, 1985; Elkind & Armentrout, 1986; Elkind & Armentrout, 1986; Elkind & Armentrout, 1986; Elkind & Armentrout, 1987; Elkind &

Armentrout, 1987; Elkind & Armentrout, 1988; Georgiadis & Armentrout, 1988; Elkind, Sunderlin & Armentrout, 1989) and 4d (Elkind, Sunderlin & Armentrout, 1989; Chen, Elkind & Armentrout, 1995; Sievers et al., 1996) TM^+ as well as many main group elemental cations (Elkind & Armentrout, 1984; Ervin & Armentrout, 1985; Ervin & Armentrout, 1986; Ervin & Armentrout, 1986; Burley, Ervin & Armentrout, 1987; Ervin & Armentrout, 1987; Ervin & Armentrout, 1989; Stowe et al., 1990; Sunderlin & Armentrout, 1994). Likewise, GIBMS studies of the 5d TM^+ are complete and include Hf^+ (Hinton & Armentrout, 2010), Ta^+ (Zhang et al., 2002), W^+ (Zhang et al., 2002), Re^+ (Armentrout & Li, 2004), Os^+ (Hinton, Citir & Armentrout, 2011), Ir^+ (Li, Zhang & Armentrout, 2005), Pt^+ (Zhang & Armentrout, 2002), and Au^+ (Li et al., 2011). GIBMS studies of reaction 5 with the lanthanides now include La^+ (Elkind, Sunderlin & Armentrout, 1989), Ce^+ (Ghiassee & Armentrout, 2020), Pr^+ (Ghiassee, Ewigleben & Armentrout, 2020), Nd^+ (Ghiassee & Armentrout, 2021), Sm^+ (Demireva & Armentrout, 2018), Gd^+ (Demireva & Armentrout, 2018), and Lu^+ (Elkind, Sunderlin & Armentrout, 1989) along with the actinide Th^+ (Cox, Armentrout & de Jong, 2016). In nearly all of these studies, reactions of H_2, HD, and D_2 were compared, which provides more robust thermochemistry because the same BDE is measured in multiple systems given that zero-point energy corrections are easily applied. Further, the reaction with HD provides dynamic information from the ratio of $MH^+ + D$ to $MD^+ + H$ products, as described in detail elsewhere (Elkind & Armentrout, 1987).

Results for the 5d TM^+ are summarized in Figure 6a. It can be seen that the range of threshold energies is much more modest compared to the oxidation reactions, spanning from about 0.8 to 1.6 eV. Ir^+ and Pt^+ have the lowest threshold energies and Au^+ has the highest, followed closely by Ta^+, W^+, Re^+, and Hf^+. Maximum magnitudes of the cross sections occur at $D_0(H_2)$ = 4.478 eV (Ruscic & Bross, 2019) and again are fairly similar (within a factor of 3) for all metal cations. Analogous similarities are found for the lanthanides and Th^+ in Figure 6b. (Results for the D_2 isotopologue are shown because they provide the same information as H_2 reactions with better mass resolution and thus less noise.) Here, the lanthanide thresholds are clustered around 1.5 – 2.0 eV, with that for Th^+ somewhat lower (comparable to Ta^+). Again the cross sections peak near

$D_0(D_2)$ = 4.556 eV.

VII. THERMOCHEMISTRY

A. Lanthanides

Bohme and co-workers have previously shown that the LnO^+ BDEs correlate well with the promotion energy needed to achieve a $5d^16s^1$ electron configuration on Ln^+, $E_p(5d^16s^1)$, although the correlation differs for the early (La - Sm) and late lanthanides (Eu - Lu) (Koyanagi & Bohme, 2001). In a systematic exploration of the neutral and cationic oxide BDEs of lanthanides and actinides, Gibson considered promotion energies to both $5d^16s^1$ and $5d^2$ configurations, showing that the latter provides a better correlation (Gibson, 2003). Comparisons using updated BDEs are shown in Figure 7. Correlation with the $5d^2$ configuration has an R^2 value of 0.96, whereas that for $5d^16s^1$ is 0.83. Further, a correlation using a slope of negative unity (dashed line) provides almost as good a reproduction of the $E_p(5d^2)$ data. Calculations on LnO^+ clearly show that these molecules have a triple bond ($1\sigma^21\pi^4$) formed by combinations of the 2p orbitals (with four electrons) on oxygen with 5d orbitals (and two electrons) on the lanthanide cation (Demireva, Kim & Armentrout, 2016; Armentrout & Cox, 2017; Ghiassee, Kim & Armentrout, 2019; Ghiassee, Stevenson & Armentrout, 2021). There is little 6s character in the sigma bond, consistent with the correlation to the $5d^2$ electronic configuration. All remaining valence electrons reside in 4f orbitals, such that the LnO^+ valence configurations correspond to $1\sigma^21\pi^4$ [$4f^n$].

In addition to the correlations considered by Bohme and Gibson, it is also reasonable to consider correlations with other charge states of the asymptote. Recently, Morse and co-workers have shown a very good correlation of neutral lanthanide oxide, sulfide, and selenide (LnX where X = O, S, and Se) BDES with promotion energies to the $Ln^+(5d^16s^1)$ + X^- dissociation limit (Sorensen, Tieu & Morse, 2021). In this same vein, Figure 7 shows an analogous correlation between $D_0(LnO^+)$ and the energy needed to dissociate to form $Ln^{2+}(5d^1)$ + O^-, i.e., $IE(Ln^+)$ + $E_p(Ln^{2+}, 5d^1)$ – $EA(O^-)$, where $E_p(Ln^{2+}, 5d^1)$ is the promotion energy needed to take ground state Ln^{2+} to a configuration having a single 5d electron and EA is the electron affinity of O, 1.461 eV

(Ruscic & Bross, 2019). These IE and E_p values were taken from (Kramida et al., 2012). The plot in Figure 7, which has an intercept of 18.53 eV, also arbitrarily subtracts 9 eV from the correlation in order to put it on the same scale as the other two correlations. As can be seen, this correlation ($R^2 = 0.98$) is slightly better than that for $E_p(5d^2)$, and naturally has a slope of -1.00. The only point that deviates significantly from the line is that for EuO^+, potentially indicating this BDE value is somewhat low or that the very stable half-filled $4f^7$ shell in Eu^{2+} leads to a different bonding configuration. Notably, Morse and co-workers found Eu (and Sm) were anomalous in their correlations as well (Sorensen, Tieu & Morse, 2021). Importantly, this correlation indicates that electronic configuration of LnO^+ remains the same as that derived from $E_p(Ln^+,5d^2)$, i.e., a triple bond ($1\sigma^2 1\pi^4$) formed using O (2p) and Ln (5d) orbitals; however, the correlation suggests that the LnO^+ molecules probably have some ionic character.

Figure 8 shows the lanthanide oxide cation BDEs measured using GIBMS experiments, along with those for the carbides, dioxides, and hydrides. To the author's knowledge, information on the latter species is not available for the remaining lanthanides, certainly at the level of the present compilation. Because the LnO^+ bonds are all strong, reactions with O_2 to form LnO^+ are exothermic, as indicated by the dashed line in Figure 8. Clearly, the LnC^+ and LnO_2^+ BDEs are much weaker than those for LnO^+, but the pattern across the periodic table remains similar. Thus, the same promotion energy arguments discussed above appear to hold for these species. For the carbides, calculations indicate that the LnC^+ molecules form by combining the 2p orbitals (two electrons) on carbon with 5d orbitals (two electrons) on the lanthanide cation. This leads to $1\sigma^1 1\pi^3$ valence configurations for LnC^+ with a bond order of two and the same number of 4f electrons as the analogous LnO^+ molecules (Demireva, Kim & Armentrout, 2016; Ghiassee, Kim & Armentrout, 2019; Ghiassee, Stevenson & Armentrout, 2021). Given the bond orders of LnC^+ and LnO^+, one might have expected that the carbide BDEs would be about two-thirds of the oxide BDEs; whereas the ratio is closer to one half. (For Pr, Nd, and Gd, the BDE ratio of MC^+/MO^+ is 0.45, whereas that for Sm is 0.58 (Ghiassee, Stevenson & Armentrout, 2021).) This difference can be attributed to the higher electronegativity of O versus C, which stabilizes the valence bonding

molecular orbitals in the oxides. Finally, we note that the BDE for CeC^+ is comparable to that for PrC^+ even though the promotion energy arguments (and parallels with LnO^+) would suggest it should be substantially larger. Given the large uncertainty in the CeC^+ BDE, these observations suggest that the true value probably lies close to the experimental upper limit.

For the dioxides, the additional oxygen contributes four more electrons to the bonding but no more electrons are contributed by the lanthanide. Because the two oxygen ligands share the two 5d electrons on Ln^+, the bond order is half that of the monoxides, consistent with the energies observed. For PrO_2^+ and NdO_2^+, the molecules are linear with valence electronic configurations of $\sigma_g^2\pi_g^4\pi_u^4$, where the orbitals resemble those of CO_2, except the nonbonding π_u orbitals have a small amount of 4f character (Ghiassee, Kim & Armentrout, 2019; Ghiassee, Stevenson & Armentrout, 2021). The same should be true of SmO_2^+, although detailed calculations have not been carried out. For GdO_2^+, the half-filled $4d^7$ shell means that the molecule prefers to be bent, with the two Gd (5d) electrons forming a bond with the two singly-occupied π_g antibonding orbitals on O_2 (Demireva & Armentrout, 2017).

In contrast to the sharp changes observed in the LnO^+, LnC^+, and LnO_2^+ BDEs moving across the periodic table, the LnH^+ BDEs vary by less than 20%. Here too, the bonding orbital on Ln^+ is a 5d, such that promotion energy arguments should again be valid, with promotion to an electronic configuration having a singly occupied 5d orbital needed. $E_p(5d^1)$ is zero for La^+ ($5d^2$), Ce^+ ($4f^15d^2$), and Gd^+ ($4f^75d^16s^1$), and these three have the strongest LnH^+ BDEs among the lanthanides, Table 1. The BDEs for the hydrides of Pr^+ ($4f^36s^1$), Nd^+ ($4f^46s^1$), and Sm^+ ($4f^66s^1$) are smaller because $E_p(5d^1)$ = 0.48, 0.63, and 0.88 eV, respectively. Notably the trend is only qualitative because the magnitude of the reduction is less than the E_p values. Mitigating factors have not been identified clearly but potentially involve the exchange energy associated with spin decoupling the 5d electron from the other valence electrons, the extent of 5d versus 6s character in the bond, and whether valence orbitals other than 4f are occupied in LnH^+ (yes for La, Ce, and Gd, but no for Pr, Nd, and Sm). For Lu^+ ($4f^{14}6s^2$) with $E_p(5d^1)$ = 1.46 eV, a smaller BDE might have been expected, which suggests that a different mode of bonding may be operational, but this

has not been investigated theoretically.

B. 5d Transition Metals

1. Oxides. Unlike the lanthanides, changes in the metal-ligand BDEs for the 5d TM^+ are not dominated by promotion energy effects, but rather by the filling of the available molecular orbitals (*MO*s) and the loss of exchange energy. For the metal oxides, it can be seen that HfO^+, TaO^+, and WO^+ BDEs are sufficiently strong to exceed $D_0(O_2)$, Figure 8, consistent with the behavior observed in Figure 1. In the case of HfO^+, the BDE is reduced because promotion from the ^2D ($5d^16s^2$) ground state to the ^4F ($5d^26s^1$) excited state (0.45 eV higher in energy (Kramida et al., 2012)) is needed to form the strong triple bond. This leads to a $^2\Sigma^+$ ground state having a $1\sigma^21\pi^42\sigma^1$ valence electronic configuration (Hinton, Li & Armentrout, 2009). Here, the *MO*s have been qualitatively described by Schröder et al. (Schröder, Schwarz & Shaik, 2000). As for the lanthanides, the 1σ and 1π orbitals are bonding *MO*s between the metal 5d and oxygen 2p orbitals. The 2σ *MO* is largely a 6s orbital on the metal along with some 5d hybridization. Low-lying orbitals are the metal 5d nonbonding 1δ *MO*s, followed by the antibonding 2π and 3σ *MO*s. For TaO^+ and WO^+, the additional electrons are placed in the 1δ *MO* leading to $^3\Delta$ ($1\sigma^21\pi^42\sigma^11\delta^1$) and $^4\Sigma^-$ ($1\sigma^21\pi^42\sigma^11\delta^2$) ground states that require no promotion (Hinton, Li & Armentrout, 2009). For ReO^+, the additional electron can be added to the 2σ, 1δ, or 2π *MO*s. Calculations indicate that both the $^3\Delta$ ($1\sigma^21\pi^42\sigma^11\delta^3$) and $^5\Pi$ ($1\sigma^21\pi^42\sigma^11\delta^22\pi^1$) states are low-lying, with corrections for spin-orbit effects suggesting the former is the true ground state (by 0.16 eV at the CCSD(T)/CBS level) (Armentrout, 2013). In either case, the BDE is reduced either by the loss of exchange energy ($^3\Delta$) or the occupation of the antibonding *MO* ($^5\Pi$). For OsO^+, the additional electron can be added to the 2π *MO* of either low-lying state of ReO^+ leading to $^4\Pi$ ($1\sigma^21\pi^42\sigma^11\delta^32\pi^1$) and $^6\Sigma^+$ ($1\sigma^21\pi^42\sigma^11\delta^22\pi^2$) states, with the former being the likely ground state once spin-orbit corrections are applied (Hinton, Citir & Armentrout, 2013). IrO^+ has a $^5\Delta$ ($1\sigma^21\pi^42\sigma^11\delta^32\pi^2$) ground state (Armentrout & Li, 2013), such that addition of the electron to the $2\pi^1$ *MO* reduces the BDE further. PtO^+, with a $^4\Sigma^-$ ($1\sigma^21\pi^42\sigma^11\delta^42\pi^2$) ground state (Heinemann, Koch & Schwarz, 1995; Zhang & Armentrout, 2003), adds an electron to the nonbonding 1δ *MO*. Here the BDE is reduced because

the $^4\Sigma^-$ state correlates with the ^{4}F ($5d^86s^1$) excited state of Pt^+, which lies 0.59 eV above the ^{2}D ($5d^9$) ground state. Finally, the closed shell Au^+ (^{1}S, $5d^{10}$) atomic cation forms a bond with oxygen in a $^3\Sigma^-$ ($1\sigma^21\pi^42\sigma^21\delta^42\pi^2$) state by adding the electron to the 2σ *MO* (Li, Gorham & Armentrout, 2010). This state correlates with an excited state of Au^+, ^{3}F ($5d^86s^2$), lying 5.02 eV above the ground state; hence, the AuO^+ BDE is particularly low.

2. Carbides. Figure 8 shows that the 5d transition metal carbide cations have BDEs that generally increase across the periodic row, in direct contrast to the behavior of the oxides. Many of these values are determined from studies of reaction 3, but some result from reactions of M^+ with alkanes. As for the lanthanides, calculations indicate that the 5d TM^+ combine 5d orbitals on the metal with 2p orbitals on carbon to form the same bonding orbitals as for the oxides, 1σ and 1π along with the nonbonding 2σ (largely 6s) and 1δ and antibonding 2π *MO*s. Of course, because C has only two p electrons, formation of a triple bond requires that the metal contribute four electrons and two of these must be low-spin coupled. This situation occurs easily for late TM^+ with either $5d^n$ or $5d^{n-1}6s^1$ configurations. Indeed, Table 1 shows the maximum MC^+ BDE occurs for IrC^+, which has a $^1\Sigma^+$ ($1\sigma^21\pi^41\delta^4$) ground state and a low-lying $^3\Delta$ ($1\sigma^21\pi^41\delta^32\sigma^1$) state (calculated as 0.14 eV higher at the CCSD(T)/CBS level) (Kim, Cox & Armentrout, 2016). The disparity between these two states arises because the former diabatically correlates with Ir^+ (^{3}F, $5d^8$), which lies 0.28 eV above the ^{5}F ($5d^76s^1$) ground state that correlates with the $^3\Delta$ state. The latter correlation favors the $^3\Delta$ state as does the higher exchange energy, but occupation of the 2σ *MO* has repulsive interactions with the bonding 1σ *MO* (as shown by a longer bond length and lower vibrational frequency: 1.671 Å and 1046 cm^{-1} for $^3\Delta$ versus 1.626 Å and 1132 cm^{-1} for $^1\Sigma^+$). For PtC^+, the additional electron yields a $^2\Sigma^+$ ($1\sigma^21\pi^41\delta^42\sigma^1$) state (Zhang & Armentrout, 2003), which correlates with excited Pt^+ (^{4}F, $5d^86s^1$), lying 0.59 eV above the ^{2}D ($5d^9$) ground state. The promotion energy and occupation of 2σ naturally lowers the BDE compared to IrC^+. Likewise, formation of the AuC^+ ground state, $^1\Sigma^+$ ($1\sigma^21\pi^41\delta^42\sigma^2$) (Li & Armentrout, 2006), requires coupling to either Au^+ (^{3}F, $5d^86s^2$) + C (^{3}P, $2p^2$) or to Au^+ (^{1}S, $5d^{10}$) + C (^{1}S, $2p^2$). The promotion energies are 5.02 and 2.68 eV, respectively, such that the latter asymptote is operative, but again

this lowers the AuC^+ BDE appreciably.

Moving to the left of IrC^+ in the periodic table, electrons are removed from the nonbonding 1δ *MO*, yielding low-lying $^4\Sigma^-$ ($1\sigma^2 1\pi^4 1\delta^2 2\sigma^1$) and $^2\Delta$ ($1\sigma^2 1\pi^4 1\delta^3$) states for OsC^+, where the latter is the ground state by 0.31 eV once spin-orbit corrections are applied (Kim, Cox & Armentrout, 2016). This latter state correlates with Os^+ (^{4}F, $5d^7$), with an excitation that has not been assigned spectroscopically. For ReC^+, the ground state is $^3\Sigma^-$ ($1\sigma^2 1\pi^4 1\delta^2$) (Kim, Cox & Armentrout, 2016), correlating with Re^+ (^{5}D, $5d^6$), which also has not been spectroscopically identified. For both OsC^+ and ReC^+, these promotion energies lead to reductions in the BDEs. For all lighter 5d TM^+, the M^+ asymptote having a $5d^n$ configuration with one 5d orbital doubly occupied is a high lying low-spin state, as the high-spin configuration is preferred because of favorable exchange energies. So for WC^+ and TaC^+, electrons are removed from the 1δ *MO*, leading to $^2\Delta$ ($1\sigma^2 1\pi^4 1\delta^1$) and $^1\Sigma^+$ ($1\sigma^2 1\pi^4$) ground states, respectively. These states diabatically correlate with low-spin M^+ states having promotion energies exceeding 3 eV. TaC^+ is also calculated to have a low-lying (within 0.1 eV) $^3\Sigma^+$ ($1\sigma^2 1\pi^3 2\sigma^1$) state (Balasubramanian, 2000; Hinton, Li & Armentrout, 2009), which correlates with the Ta^+ (^{5}F, $5d^3 6s^1$) ground state. The lack of promotion energy is compensated by the reduced bond order and repulsive 2σ *MO* occupation. Hf^+ only has three valence electrons such that it cannot form a triple bond with carbon. Its ground state is $^2\Sigma^+$ ($1\sigma^1 1\pi^4$) (Hinton, Li & Armentrout, 2009), which diabatically correlates with the Hf^+ (^{2}G, $5d^3$) excited state lying 3.48 eV above the ^{2}D ($5d^1 6s^2$) ground state, explaining its low BDE.

3. Dioxides. The ground states of TaO_2^+, WO_2^+, and ReO_2^+ have been calculated as $^1A_1$, $^2A_1$ (Hinton et al., 2011), and $^3B_1$ (Beyer et al., 1999) (a $^1A_1$ state is calculated to be 0.10 eV higher in energy) (Armentrout, 2013), respectively. All three molecules can be described as having valence configurations of $1a_1^2 1b_2^2 1a_2^2 2a_1^2 1b_1^2 2b_2^2$ with no additional electrons, an added $3a_1$ electron, and added $3a_1^1 2b_1^1$ (or $3a_1^2$) electrons, respectively. The *MO*s of MO_2^+ have been described previously (Kretzschmar et al., 1997), although they use different symmetry designations than the ones used here, which have been recommended elsewhere (Mulliken, 1955). Basically, the $1a_1$ *MO* is an in-plane π-like bonding *MO* shared by both oxygens, $1b_2$ and $2a_1$ are

the σ-like bonding *MO*s, $1a_2$ and $1b_1$ are out-of-plane π-like bonding *MO*s, $2b_2$ is a nonbonding *MO*, $3a_1$ is largely a 5dσ-6s hybrid with some antibonding character, and $2b_1$ is the antibonding analogue of $1b_1$. Thus, these three metal dioxides have ten bonding electrons and no antibonding electrons (discounting $3a_1$ as antibonding) such that the bond orders for each MO bond in all three molecules are 2.5. This explains why all three OM^+-O BDEs are similar (5.9 ± 0.3 eV) and somewhat below the triple MO^+ BDEs of ~7 eV, Figure 8.

For OsO_2^+, the core valence configuration noted above adds $3a_1^2 2b_1^1$ electrons for a $^2B_1$ ground state. The addition of the antibonding $2b_1$ electron explains why its BDE is smaller than that for ReO_2^+. IrO_2^+ adds another $2b_1$ electron, indicating its BDE should decrease further. This BDE has not been measured, but this prediction is consistent with theoretical calculations of this BDE (Kim & Armentrout, 2021). For PtO_2^+, the next electron is added into a 6s-like *MO*, which directs the molecule to be linear. Characterization of the ground state of PtO_2^+ has proven to be problematic, even using multireference approaches (Brönstrup et al., 2001; Zhang & Armentrout, 2003). Given that AuO^+ is closed shell, the OAu^+-O bond is expected to be weak and has not yet been measured.

4. Hydrides. As for the lanthanides, the BDEs of the hydrides of the 5d TM^+ do not vary appreciably across the periodic table, Figure 8. It can be seen that the values are about 1/3 those of the strongest metal oxide cation BDEs, consistent with assigning the former as single bonds and the latter as triple bonds. Periodic trends in the 5d transition metal hydride cations were predicted using generalized valence bond (GVB) theory well before experiments (except for LaH^+) were available (Ohanessian, Brusich & Goddard, 1990). The considerations outlined in that theoretical work succinctly explain the variations that are observed. Key elements are the hybridization of the metal bonding orbital and variations in the exchange energy associated with the nonbonding metal electrons. GVB theory shows that the metal bonding orbital is largely 5d, with variations in the amount of 6s character increasing from 23% at La^+ to 43% at Os^+, then back down to 11% at Pt^+, with Au^+ utilizing 30% 6s character. Exchange energies vary systematically from low values at La^+ and Au^+ to a maximum at Re^+. Promotion energy effects also occur for La^+, Hf^+, Pt^+, and Au^+.

When combined quantitatively, these factors nicely explain the periodic variations now observed experimentally, with 0 K BDEs that differ from experiment (Table 1) by a mean absolute deviation of about 0.2 eV.

C. Thorium

Figure 8 also compares the BDEs for ThH^+, ThC^+, ThO^+, and ThO_2^+ with those of the lanthanides. Thorium lies below cerium in the periodic table, such that the similarity in the oxide and hydride BDEs is not surprising. As noted above, it is expected that the CeC^+ BDE is larger than listed in Table 1, and the comparison to ThC^+ is consistent with that hypothesis. Theory shows that the bonding character of these molecules parallels that described above (Cox, Armentrout & de Jong, 2016; Cox et al., 2016).

In the case of ThO_2^+, the BDE was compared with those of the group 4 transition metal dioxide cations, TiO_2^+ and ZrO_2^+ (Armentrout & Peterson, 2020). HfO_2^+ and CeO_2^+ would also have been relevant, but BDEs for these molecules are not available. For Ti and Zr, the ratio of the first and second oxide cation BDE is almost exactly one half, whereas for ThO_2^+, the $D_0(OTh^+\text{-}O)/D_0(Th^+\text{-}O)$ ratio is 0.58. As alluded to above, the 0.50 ratio makes sense because the bond order in these systems changes from 3 for the monoxide to 1.5 for the dioxide. The 8% enhancement observed for Th was attributed to the contribution of 5f orbitals to the bonding, which could be quantitatively estimated as 1.5 eV for two 5fπ bonds and one electron in 5fσ bond. Although appreciable from a thermodynamic point of view, such interactions are still weaker than Th (5d) – O (2p) covalent bonds, which are worth about 2.8 eV each. Theory is consistent with this experimental analysis and finds that the 5f orbital participation leads to a linear molecule for ThO_2^+ (Wadt, 1981; Dyall, 1999), in contrast to bent species for TiO_2^+ and ZrO_2^+. Figure 9 shows the $1\pi_u$ (doubly occupied degenerate orbitals) and $1\sigma_u$ (singly occupied) *MO*s for ThO_2^+.

VIII. CHEMI-IONIZATION

Our recent efforts to examine the oxidation thermochemistry of the lanthanides in a systematic fashion is motivated by an interesting atmospheric problem. Satellite communication

utilizes radio waves that pass through the ionosphere twice, once on the way to the satellite and then back again to the target. Discontinuities in the plasma density can grow to sizes where the imperfections refract the radio waves, disrupting communication for many seconds, a dropout in signal known as scintillation. The U. S. Air Force is interested in mediating scintillation and has explored the use of spontaneous chemi-ionization (CI) reactions, e.g., reaction 6.

$$M + O \rightarrow MO^+ + e^- \qquad (6)$$

Oxygen atoms are abundant in the ionosphere and act as a ready reagent. Reaction 6 is clearly unusual, which can be attributed to the fact that for this reaction to be exothermic, $\Delta_{CI}H < 0$, it requires that the BDE of MO, $D_0(MO)$, exceed the ionization energy of MO, IE(MO): $\Delta_{CI}H = IE(MO) - D_0(MO)$. For most species, IEs are usually much larger than their BDEs, so reaction 6 requires a strong bond and a low IE. The latter requirement implicates a metal and the former means a triple bond is needed. As detailed above, early transition metals and, by extension, many lanthanides and actinides can form the strong triple bond with oxygen and also have relatively low IEs. It has been known since the 1970's that such CI reactions do occur with reasonable cross sections (Fite, Lo & Irving, 1974; Lo & Fite, 1974; Fite, Patterson & Siegel, 1976). More recent work has documented this further for several lanthanides (Ard et al., 2015; Ard et al., 2016).

In 2013, the Air Force Research Laboratory (AFRL) put this idea to an atmospheric test in the Metal Oxide Space Cloud (MOSC) experiment (Bernhardt et al., 2017; Caton et al., 2017). Sounding rockets containing 6 kg of samarium (Sm) coupled to a thermite reactor were launched above an atoll in the Republic of the Marshall Islands, and the thermite was ignited at altitudes near 170 and 180 km. A pink cloud, 10 – 50 km in diameter (Retterer et al., 2017), was observed from land-based observation sites attesting to some reaction between Sm and the atmosphere. The cloud persisted for several hours. A number of land-based measurements were made and carefully monitored the characteristics of the cloud. Many aspects of the reaction did not achieve pre-flight predictions; in particular, the artificial plasma density was about an order of magnitude smaller than expected. To understand this problem, it seemed clear that better information about the CI reaction was needed. At the time, literature thermochemistry, reviewed thoroughly in (Cox et al.,

2015), indicated that $D_0(SmO) = 5.88 \pm 0.17$ eV (Pedley & Marshall, 1983) and IE(SmO) = 5.55 ± 0.10 eV (Ackermann, Rauh & Thorn, 1976), such that $\Delta_{CI}H$ (Sm) = -0.33 ± 0.20 eV.

It can be realized that the CI thermochemistry can also be obtained using different input data, namely $\Delta_{CI}H = IE(M) - D_0(MO^+)$. As the IE(M) values for all elements are accurately known from spectroscopic work, e.g., IE(Sm) = 5.6437 eV (Kramida et al., 2012), measurement of the MO^+ BDE is an alternate route to determine the CI thermodynamics. Therefore, studies utilizing flow tubes were pursued and demonstrated that the oxidation reaction of Sm^+ was exothermic with N_2O, NO_2, O_2 and SO_2, but was not observed for CO_2 or NO (Cox et al., 2015). These results indicate only that $D_0(OS\text{-}O) = 5.661 \pm 0.014$ eV < $D_0(SmO^+)$ < $D_0(NO) = 6.500 \pm 0.004$ eV (Johnson III, 2018), which is consistent with the literature value: $D_0(SmO^+) = D_0(SmO) - IE(SmO) + IE(Sm) = 5.88 - 5.55 + 5.6437 = 5.97 \pm 0.20$ eV. At this point, GIBMS studies were pursued to examine the reactions of Sm^+ with O_2, SO_2, CO, along with CID reactions of SmO^+ with Xe and O_2 (Cox et al., 2015). Three reactions provided three useful values for $D_0(SmO^+)$, which yielded a weighted average final value of $5.72_5 \pm 0.07$ eV. When combined with IE(Sm), this indicates $\Delta_{CI}H$ = -0.08 ± 0.07 eV, less exothermic than the literature value. In parallel, IE(SmO) was remeasured using pulsed field ionization zero kinetic energy photoelectron spectroscopy, yielding a value of 5.7427 ± 0.0006 eV (Cox et al., 2015). Combined with the literature value for $D_0(SmO)$, this indicates that $\Delta_{CI}H = -0.14 \pm 0.17$ eV, showing that the value obtained using $D_0(SmO^+)$ is accurate.

The reason that this subtle difference in CI exothermicities makes such a difference in the atmospheric observations is related to the reverse dissociative recombination reaction (reforming M + O), the reverse of reaction 6. Clearly, the cation and electron are strongly attracted by Coulomb forces such that the reverse process potentially has a very large cross section, but the reverse reaction can only occur if there is enough energy. Thus, if the CI reaction is exothermic, then the reverse process can only occur if the electron is energetic enough (or if the SmO^+ has internal excitation). At an elevation of ~200 km, electrons have a kinetic energy distribution reasonably described as Maxwellian at about 1000 K. If the CI reaction is exothermic by 0.33 eV, then few electrons are energetic enough to induce dissociative recombination; whereas if $\Delta_{CI}H$

= -0.07 eV, then a large fraction of the electrons can induce the reverse process limiting ionization to about 10% (Caton et al., 2017). This explains the order of magnitude difference in the expected plasma density observed in the atmospheric tests.

One fascinating aspect of the CI experiment is that there is an inverse correlation between $\Delta_{CI}H$ and the boiling point of the metal (or enthalpies of vaporization), or viewed differently, the stronger the metal-metal interactions are, the stronger the metal-oxygen interactions are (which increases the exothermicity of reaction 6). Thus, lanthanides whose CI reactions are strongly exothermic are lanthanides with high boiling points. Sm has been used for most atmospheric tests to date because the CI reaction was thought to be exothermic enough, and it has a relatively low boiling point, only 2173 K, and low vaporization enthalpy (2.0 eV) (Zhang, Evans & Yang, 2011). In contrast, La, Ce, Pr, Nd, and Gd, which all have much stronger LnO and LnO^+ BDEs (see Figure 8 and Table 1), have boiling points exceeding 3273 K and $\Delta_{vap}H$ values exceeding 3.0 eV. From a practical point of view, efficient vaporization of the metal is required to generate metal atoms as the reactant for the CI reaction 6. Therefore, locating a metal that strikes a balance between the exothermicity of the CI reaction and the ease of its vaporization is needed.

ACKNOWLEDGEMENT

I thank my students whose names appear in the references for their considerable contributions to the work reviewed here. The 5d TM^+ chemistry has been funded by the National Science Foundation (CHE-1954142), lanthanide chemistry by the Air Force Office of Scientific Research (FA9550-20-1-0329), and thorium chemistry by the Department of Energy, Office of Basic Energy Sciences, Heavy Element Chemistry Program (DE-SC0012249).

REFERENCES

Ackermann RJ, Rauh EG, Thorn RJ. The thermodynamics of ionization of gaseous oxides; the first ionization potentials of the lanthanide metals and monoxides. 1976. J. Chem. Phys. 65:1027-1031.

Aguirre F, Husband J, Thompson CJ, Metz RB. Gas-phase Photodissociation of $AuCH_2^+$: The Dissociation Threshold of Jet-cooled and Rotationally Thermalized Ions. 2000. Chem. Phys. Lett. 318:466-470.

Ard SG, Shuman NS, Martinez O, Armentrout PB, Viggiano AA. Chemi-ionization reactions of La, Pr, Tb, and Ho with atomic O and La with N_2O from 200 - 450 K. 2016. J. Chem. Phys. 145:084302.
Ard SG, Shuman NS, O. Martinez J, Brumbach MT, Viggiano AA. Kinetics of chemi-ionization reactions of lanthanide metals (Nd, Sm) from 150 to 450 K. 2015. J. Chem. Phys. 143:204303.
Aristov N, Armentrout PB. Reaction Mechanisms and Thermochemistry of $V^+ + C_2H_{2p}$ (p = 1,2,3). 1986. J. Am. Chem. Soc. 108:1806-1819.
Aristov N, Armentrout PB. Methane Activation by V^+: Electronic and Translational Energy Dependence. 1987. J. Phys. Chem. 91:6178-6188.
Armentrout PB. Periodic trends in the reactions of atomic ions with molecular hydrogen. 1990. Int. Rev. Phys. Chem. 9:115-148.
Armentrout PB. 1992. Thermochemical Measurements by Guided Ion Beam Mass Spectrometry. In: Adams N, Babcock LM, Editors. Adv. Gas Phase Ion Chem. Greenwich, Connecticut: JAI Press. p 83-119.
Armentrout PB. The Kinetic Energy Dependence of Ion-Molecule Reactions: Guided Ion Beams and Threshold Measurements. 2000. Int. J. Mass Spectrom. 200:219-241.
Armentrout PB. Not Just a Structural Tool: The Use of Guided Ion Beam Tandem Mass Spectrometry to Determine Thermochemistry. 2002. J. Am. Soc. Mass Spectrom. 13:419-434.
Armentrout PB. The Bond Energy of ReO^+: Guided Ion-Beam and Theoretical Studies of the Reaction of Re^+ (^7S) with O_2. 2013. J. Chem. Phys. 139:084305.
Armentrout PB. Methane Activation by 5d Transition Metals: Energetics, Mechanisms, and Periodic Trends. 2017. Chem.: Eur. J. 23:10-18.
Armentrout PB, Botero J. 1995. Particle Interchange Reactions Involving Plasma Impurity Ions and H_2, D_2 and HD. In: Janev RK, Editor Atomic and Molecular Processes in Fusion Edge Plasmas. New York: Plenum. p 433-460.
Armentrout PB, Chang Y-C, Ng C-Y. What is the Bond Dissociation Energy of the Vanadium Hydride Cation? 2020. J. Phys. Chem. A 124:5306-5313.
Armentrout PB, Cox RM. Potential Energy Surface for Reaction of $Sm^+ + CO_2 \rightarrow SmO^+ + CO$: Guided Ion Beam and Theoretical Studies. 2017. Phys. Chem. Chem. Phys. 19:11075-11088.
Armentrout PB, Cox RM, Sweeny BC, Ard SG, Shuman NS, Viggiano AA. Lanthanides as Catalysts: Guided Ion Beam and Theoretical Studies of $Sm^+ + COS$. 2018. J. Phys. Chem. A 122:737-749.
Armentrout PB, Kickel BL. 1996. Gas-Phase Thermochemistry of Transition Metal Ligand Systems: Reassessment of Values and Periodic Trends. In: Freiser BS, Editor Organometallic Ion Chemistry. Dordrecht: Kluwer. p 1-45.
Armentrout PB, Li F-X. Probes of Spin-conservation in Heavy Metal Reactions: Experimental and Theoretical Studies of the Reactions of Re^+ with H_2, D_2, and HD. 2004. J. Chem. Phys. 121:248-256.
Armentrout PB, Li F-X. Bond Energy of IrO^+: Guided Ion-Beam and Theoretical Studies of the Reaction of Ir^+ (^5F) with O_2. 2013. J. Phys. Chem. A 117:7754-7766.
Armentrout PB, Peterson KA. Guided Ion Beam and Quantum Chemical Investigation of the Thermochemistry of Thorium Dioxide Cations: Thermodynamic Evidence for Participation of *f* Orbitals in Bonding. 2020. Inorg. Chem. 59:3118-3131.
Balasubramanian K. Spectroscopic constants and potential energy curves of tungsten carbide. 2000. J. Chem. Phys. 112:7425-7436.
Bernhardt PA, Siefring CL, Briczinski SJ, Viggiano A, Caton RG, Pedersen TR, Holmes JM,

Ard S, Shuman N, Groves KM. A Physics-based Model for the Ionization of Samarium by the MOSC Chemical Releases in the Upper Atmosphere. 2017. Radio Science 52:559-577.
Beyer M, Berg C, Joos S, Achatz U, Hieringer W, Niedner-Schatteburg G, Bondybey VE. The $[Re, O_8]^+$ potential energy surface: fourier transform ion cyclotron resonance collision induced dissociation studies and density functional calculations. 1999. Int. J. Mass Spectrom. 185-187:625-638.
Blagojevic V, Bohme DK. ICP-SIFT/MS study of gas-phase reactions of atomic metal cations with pyridine at room temperature: Kinetics and periodicities in reactivity. 2015. Int. J. Mass Spectrom. 377:484-489.
Blagojevic V, Flaim E, Jarvis MJY, Koyanagi GK, Bohme DK. Nitric Oxide as an Electron Donor, an Atom Donor, an Atom Acceptor, and a Ligand in Reactions with Atomic Transition-Metal and Main-Group Cations in the Gas Phase. 2005. J. Phys Chem. A 109:11224-11235.
Blagojevic V, Lavrov VV, Koyanagi GK, Bohme DK. Early atomic transition metal cations reacting with ammonia at room temperature: H_2 elimination and NH_3 ligation kinetics across and down the periodic table. 2019. Int. J. Mass Spectrom. 435:181-187.
Blagojevic V, Lavrov VV, Koyanagi GK, Bohme DK. Ligation kinetics as a probe for gas-phase ligand field effects: Ligation of atomic transition metal cations with ammonia at room temperature. 2019. Eur. J. Mass Spectrom. 25:44-49.
Brönstrup M, Schröder D, Kretzschmar I, Schwarz H, Harvey JN. Platinum Dioxide Cation: Easy to Generate Experimentally but Difficult to Describe Theoretically. 2001. J. Am. Chem. Soc. 123:142-147.
Burley JD, Ervin KM, Armentrout PB. Translational Energy Dependence of $O^+(^4S) + H_2(D_2, HD) \rightarrow OH^+(OD^+) + H(D)$ from Thermal to 30 eV c.m. 1987. Int. J. Mass Spectrom. Ion Processes 80:153-175.
Caraiman D, Koyanagi GK, Bohme DK. Gas-Phase Reactions of Transition-Metal Ions with Hexafluorobenzene: Room-Temperature Kinetics and Periodicities in Reactivity. 2004. J. Phys. Chem. A 108:978-986.
Caton RG, Pedersen TR, Groves KM, Hines J, Cannon PS, Jackson-Booth N, Parris RT, Holmes JM, Su Y-J, Mishin EV, Roddy PA, Viggiano AA, Shuman NS, Ard SG, Bernhardt PA, Siefring CL, Retterer J, Kudeki E, Reyes PM. Artificial Ionospheric Modification: The Metal Oxide Space Cloud Experiment. 2017. Radio Science 52:539-558.
Chen Y-M, Armentrout PB. Kinetic Energy Dependence of the Reactions of Ru^+, Rh^+, Pd^+, and Ag^+ with O_2. 1995. J. Chem. Phys. 103:618-625.
Chen Y-M, Elkind JL, Armentrout PB. Reactions of Ru^+, Rh^+, Pd^+, and Ag^+ with H_2, HD and D_2. 1995. J. Phys. Chem. 99:10438-10445.
Cheng P, Bohme DK. Gas-Phase Reactions of Atomic Lanthanide Cations with Sulfur Hexafluoride: Periodicity in Reactivity. 2006. Inorg. Chem. 45:7856-7863.
Cheng P, Koyanagi GK, Bohme DK. Carbon Disulfide Reactions with Atomic Transition-Metal and Main-Group Cations: Gas-Phase Room-Temperature Kinetics and Periodicities in Reactivity. 2006b. J. Phys. Chem. A 110:2718-2728.
Cheng P, Koyanagi GK, Bohme DK. Gas-Phase Reactions of Atomic Lanthanide Cations with CO_2 and CS_2: Room-Temperature Kinetics and Periodicities in Reactivity. 2006a. J. Phys. Chem. A 110:12832-12838.
Cheng P, Koyanagi GK, Bohme DK. Gas-Phase Reactions of Atomic Lanthanide Cations with D_2O: Room-Temperature Kinetics and Periodicity in Reactivity. 2006c. ChemPhysChem 7:1813-1819.

Cheng P, Koyanagi GK, Bohme DK. Heavy Water Reactions with Atomic Transition-Metal and Main-Group Cations: Gas Phase Room-Temperature Kinetics and Periodicities in Reactivity. 2007. J. Phys. Chem. A 111:8561-8573.
Cheng P, Shayesteh A, Bohme DK. Gas-phase reactions of sulfur hexafluoride with transition metal and main group atomic cations: room-temperature kinetics and periodicities in reactivity. 2009. Inorg. Chem. 48:1018-1029.
Clemmer DE, Chen Y-M, Khan FA, Armentrout PB. State-Specific Reactions of $Fe^+(a^6D, a^4F)$ with D_2O and Reactions of FeO^+ with D_2. 1994. J. Phys. Chem. 98:6522-6529.
Clemmer DE, Weber ME, Armentrout PB. Reactions of $Al^+(^1S)$ with NO_2, N_2O and CO_2: Thermochemistry of AlO and AlO^+. 1992. J. Phys. Chem 96:10888-10893.
Cornehl HH, Wesendrup R, Diefenbach M, Schwarz H. A Comparative Study of Oxo-Ligand Effects in the Gas-Phase Chemistry of Atomic Lanthanide and Actinide Cations. 1997. Chem. Eur. J. 3:1083-1090.
Cox RM, Armentrout PB, de Jong WA. Reactions of $Th^+ + H_2$, D_2, and HD Studied by Guided Ion Beam Tandem Mass Spectrometry and Quantum Chemical Calculations. 2016. J. Phys. Chem. B 120:1601-1614.
Cox RM, Citir M, Armentrout PB, Battey SR, Peterson KA. Bond Energies of ThO^+ and ThC^+: A Guided Ion Beam and Quantum Chemical Investigation of the Reactions of Thorium Cation with O_2 and CO. 2016. J. Chem. Phys. 144:184309.
Cox RM, Kim J, Armentrout PB, Bartlett J, VanGundy RA, Heaven MC, Ard SG, Melko JJ, Shuman NS, Viggiano AA. Evaluation of the Exothermicity of the Chemi-ionization Reaction $Sm + O \rightarrow SmO^+ + e^-$. 2015. J. Chem. Phys. 142:134307.
Daly NR. Scintillation Type Mass Spectrometer Ion Detector. 1960. Rev. Sci. Instrum. 31:264-267.
Demireva M, Armentrout PB. Gadolinium Cation (Gd^+) Reaction with O_2: Potential Energy Surface Mapped Experimentally and with Theory. 2017. J. Chem. Phys. 146:174302.
Demireva M, Armentrout PB. Activation of CO_2 by Gadolinium Cation (Gd^+): Energetics and Mechanism from Experiment and Theory. 2018. Top. Catal. 61:3-19.
Demireva M, Armentrout PB. Activation of H_2 by Gadolinium Cation (Gd^+): Bond Energy of GdH^+ and Mechanistic Insights from Guided Ion Beam and Theoretical Studies. 2018. J. Phys. Chem. A 122:750-761.
Demireva M, Armentrout PB. Samarium Cation (Sm^+) Reactions with H_2, D_2, and HD: SmH^+ Bond Energy and Mechanistic Insights from Guided Ion Beam and Theoretical Studies 2018. J. Chem. Phys. 149:164304.
Demireva M, Kim J, Armentrout PB. Gadolinium (Gd) Oxide, Carbide, and Carbonyl Cation Bond Energies and Evaluation of the $Gd + O \rightarrow GdO^+ + e^-$ Chemi-Ionization Reaction Enthalpy. 2016. J. Phys. Chem. A 120:8550-8563.
Dotan I, Lindinger W. Energy dependencies of the reactions of Ar^+ with H_2, N_2, CO, O_2, CO_2, N_2O, and COS. 1982. J. Chem. Phys. 76:4972-4977.
Dyall KG. Bonding and bending in the actinyls. 1999. Molec. Phys. 96:511-518.
Elkind JL, Armentrout PB. Threshold Behavior for Chemical Reactions: Line of Centers Cross Section for $Si^+(^2P) + H_2 \rightarrow SiH^+ + H$. 1984. J. Phys. Chem. 88:5454-5456.
Elkind JL, Armentrout PB. Effect of Kinetic and Electronic Energy on the Reaction of V^+ with H_2, HD and D_2. 1985. J. Phys. Chem. 89:5626-5636.
Elkind JL, Armentrout PB. Effect of Kinetic and Electronic Energy on the Reactions of Co^+, Ni^+ and Cu^+ with H_2, HD and D_2. 1986c. J. Phys. Chem. 90:6576-6586.

Elkind JL, Armentrout PB. Effect of Kinetic and Electronic Energy on the Reactions of Fe^+ with H_2, HD and D_2: State-Specific Cross Sections for $Fe^+(^6D)$ and $Fe^+(^4F)$. 1986b. J. Phys. Chem. 90:5736-5745.
Elkind JL, Armentrout PB. Effect of Kinetic and Electronic Energy on the Reactions of Mn^+ with H_2, HD and D_2 1986a. J. Chem. Phys. 84:4862-4871.
Elkind JL, Armentrout PB. Transition Metal Hydride Bond Energies: First and Second Row. 1986d. Inorg. Chem. 25:1078-1080.
Elkind JL, Armentrout PB. Effect of Kinetic and Electronic Energy on the Reactions of Cr^+ with H_2, HD and D_2. 1987a. J. Chem. Phys. 86:1868-1877.
Elkind JL, Armentrout PB. State-specific Reactions of Atomic Transition Metal Ions with H_2, HD and D_2: Effects of d Orbitals on Chemistry. 1987b. J. Phys. Chem. 91:2037-2045.
Elkind JL, Armentrout PB. Effect of Kinetic and Electronic Energy on the Reactions of Ti^+ with H_2, HD and D_2. 1988. Int. J. Mass Spectrom. Ion Processes 83:259-284.
Elkind JL, Sunderlin LS, Armentrout PB. Periodic Trends in Chemical Reactivity: Reactions of Sc^+, Y^+, La^+, and Lu^+ with H_2, D_2, and HD. 1989. J. Phys. Chem. 93:3151-3158.
Ervin KM, Armentrout PB. Translational Energy Dependence of $Ar^+ + XY \rightarrow ArX^+ + Y$ (XY = H_2, D_2, HD) from Thermal to 30 eV c.m. 1985. J. Chem. Phys. 83:166-189.
Ervin KM, Armentrout PB. $C^+(^2P) + H_2(D_2,HD) \rightarrow CH^+(CD^+) + H(D)$. I. Reaction Cross Sections and Kinetic Isotope Effects from Threshold to 15 eV c.m. 1986. J. Chem. Phys. 84:6738-6749.
Ervin KM, Armentrout PB. Spin-orbit State-selected Reactions of $Kr^+(^2P_{3/2}$ and $^2P_{1/2})$ with H_2, D_2, and HD from Thermal Energies to 20 eV c.m. 1986. J. Chem. Phys. 85:6380-6395.
Ervin KM, Armentrout PB. Energy dependence, kinetic isotope effects, and thermochemistry of the nearly thermoneutral reactions of $N^+ + H_2 \rightarrow NH^+ + H$. 1987. J. Chem. Phys. 86:2659-2673.
Ervin KM, Armentrout PB. Spin Orbit State selected Reactions of $Xe^+(^2P_{3/2}$ and $^2P_{1/2})$ with H_2, D_2, and HD. 1989. J. Chem. Phys. 90:118-126.
Fisher ER, Elkind JL, Clemmer DE, Georgiadis R, Loh SK, Aristov N, Sunderlin LS, Armentrout PB. Reactions of Fourth Period Metal Ions (Ca^+ - Zn^+) with O_2: Metal Oxide Ion Bond Energies. 1990. J. Chem. Phys. 93:2676-2691.
Fite WL, Lo HH, Irving P. Associative Ionization in U + O and U + O_2 Collisions. 1974. J. Chem. Phys. 60:1236-1250.
Fite WL, Patterson TA, Siegel MW. 1976. Cross Sections for Thermal Reactions Between Uranium Atoms and Atmospheric Species. Air Force Geophysics Laboratory, Hanscom Air Force Base MA, Report No. AFGL-TR-77-0030, NTIS Access No. AD/A 038806. p 1-88.
Gaucherel P, Rowe B. Measurement of rates of charge exchange and dissociative recombination reactions in $Ar{\cdot}N_2$, $Ar{\cdot}H_2$ and $Ar{\cdot}O_2$ mixtures. 1977. Int. J. Mass Spectrom. Ion Phys. 25:211-227.
Georgiadis R, Armentrout PB. Kinetic Energy Dependence of the Reactions of Ca+ and Zn+ with H2, D2, and HD. Effect of Empty versus Full d Orbitals. 1988. J. Phys. Chem 92:7060-7067.
Gerlich D. 1992. Inhomogeneous rf Fields: A Versatile Tool for the Study of Processes with Slow Ions. In: Ng C-Y, Baer M, Editors. Adv. Chem. Phys.: Wiley. p 1-176.
Ghiassee M, Armentrout PB. Cerium Cation (Ce+) Reactions with H2, D2, and HD: CeH+ Bond Energy and Mechanistic Insights from Guided Ion Beam and Theoretical Studies. 2020. J. Phys. Chem. A 124:2560-2572.
Ghiassee M, Armentrout PB. Activation of D_2 by Neodymium Cation (Nd^+): Bond Energy of NdH^+ and Mechanistic Insights through Experimental and Theoretical Studies 2021. J. Phys.

Chem. A:submitted for publication.
Ghiassee M, Ewigleben J, Armentrout PB. Praseodymium cation (Pr^+) reactions with H_2, D2, and HD: PrH^+ bond energy and mechanistic insights from guided ion beam and theoretical studies. 2020. J. Chem. Phys. 153:144304.
Ghiassee M, Kim J, Armentrout PB. Evaluation of the exothermicity of the chemi-ionization reaction Nd + O → $NdO^+ + e^-$ and neodymium oxide, carbide, dioxide, and carbonyl cation bond energies. 2019. J. Chem. Phys. 150:144309.
Ghiassee M, Stevenson BC, Armentrout PB. Evaluation of the Pr + O → $PrO^+ + e^-$ Chemi-ionization Reaction Enthalpy and Praseodymium Oxide, Carbide, Dioxide, and Carbonyl Cation Bond Energies. 2021. Phys. Chem. Chem. Phys.:accepted for publication.
Gibson JK. Role of Atomic Electronics in f-Element Bond Formation: Bond Energies of Lanthanide and Actinide Oxide Molecules. 2003. J. Phys. Chem. A 107:7891-7899.
Gingerich KA. Mass-Spectrometric Evidence for the Molecules UC and CeC and Predicted Stability of Diatomic Carbides of Electropositive Transition Metals. 1969. J. Chem. Phys. 50:2255-2256.
Gioumousis G, Stevenson DP. Reactions of Gaseous Molecule Ions with Gaseous Molecules. V. Theory. 1958. J. Chem. Phys. 29:294-299.
Haynes CL, Armentrout PB. Thermochemistry and Structures of $CoC_3H_6^+$: Metallacycle and Metal-Alkene Isomers. 1994. Organomet. 13:3480-3490.
Heinemann C, Koch W, Schwarz H. An approximate method for treating spin-orbit effects in platinum. 1995. Chem. Phys. Lett. 245:509-518.
Henglein A. Stripping effects in ion−molecule reactions. 1966. Adv. Chem. Ser. 58:63-79.
Hinton CS, Armentrout PB. Guided Ion Beam and Theoretical Study of the Reactions of Hf^+ with H_2, D_2, and HD 2010. J. Chem. Phys. 133:124307.
Hinton CS, Citir M, Armentrout PB. Guided Ion Beam and Theoretical Study of the Reactions of Os^+ with H_2, D_2, and HD. 2011. J. Chem. Phys. 135:234302.
Hinton CS, Citir M, Armentrout PB. Guided Ion-Beam and Theoretical Studies of the Reaction of Os^+ (^6D) with O_2: Adiabatic and Nonadiabatic Behavior. 2013. Int. J. Mass Spectrom. 354-355:87-98.
Hinton CS, Citir M, Manard M, Armentrout PB. Collision-induced Dissociation of MO^+ and MO_2^+ (M = Ta and W): Metal Oxide and Dioxide Cation Bond Energies. 2011. Int. J. Mass Spectrom. 308:265-274.
Hinton CS, Li F-X, Armentrout PB. Reactions of Hf^+, Ta^+, and W^+ with O_2 and CO: Metal Carbide and Metal Oxide Cation Bond Energies. 2009. Int. J. Mass Spectrom. 280:226-234.
Jarvis MJY, Blagojevic V, Koyanagi GK, Bohme DK. Nitrogen Dioxide Reactions with Atomic Lanthanide Cations and Their Monoxides: Gas-phase Kinetics at Room Temperature. 2010. Phys. Chem. Chem. Phys. 12:4852-4862.
Jarvis MJY, Blagojevic V, Koyanagi GK, Bohme DK. Nitrogen Dioxide Reactions with 46 Atomic Main-Group and Transition Metal Cations in the Gas phase: Room Temperature Kinetics and Periodicities in Reactivity. 2013. J. Phys. Chem. A 117:1151-1157.
Johnson III RD. 2018. NIST Computational Chemistry Comparison and Benchmark Database. In: Russell DJ, III, Editor NIST Standard Reference Database Number 101, Release 19. NIST Computational Chemistry Comparison and Benchmark Database.
Kickel BL, Armentrout PB. Guided Ion Beam Studies of the Reactions of Group 3 Metal Ions (Sc^+, Y^+, La^+, and Lu^+) with Silane. Electronic State Effects, Comparison to Reactions with Methane, and M^+-SiH_x (x = 0 - 3) Bond Energies. 1995. J. Am. Chem. Soc. 117:4057-4070.

Kickel BL, Armentrout PB. Reactions of Fe^+, Co^+ and Ni^+ with Silane. Electronic State Effects, Comparison to Reactions with Methane, and M^+-SiH_x (x = 0 - 3) Bond Energies. 1995. J. Am. Chem. Soc. 117:764-773.
Kim J, Armentrout PB. Guided Ion Beam Tandem Mass Spectrometry and Theoretical Study of SO_2 Activated by Os^+ 2020. J. Phys. Chem. A 124:6629-6644.
Kim J, Armentrout PB. Thermochemistry of $Ir^+ + SO_2$ Reaction using Guided Ion Beam Tandem Mass Spectrometry and Theory. 2021. J. Chem. Phys.:accepted for publication.
Kim J, Cox RM, Armentrout PB. Guided Ion Beam and Theoretical Studies of the Reactions of Re^+, Os^+, and Ir^+ with CO. 2016. J. Chem. Phys. 145:194305.
Kim J, Cox RM, Armentrout PB. Thermochemical Studies of Reactions of Re^+ with SO_2 Using Guided Ion Beam Experiments and Theory. 2020. Phys. Chem. Chem. Phys. 22:3191-3203.
Koyanagi GK, Bohme DK. Oxidation Reactions of Lanthanide Cations with N_2O and O_2: Periodicities in Reactivity. 2001. J. Phys. Chem. A 105:8964-8968.
Koyanagi GK, Bohme DK. Gas-Phase Reactions of Carbon Dioxide with Atomic Transition-Metal and Main-Group Cations: Room-Temperature Kinetics and Periodicities in Reactivity. 2006. J. Phys. Chem. A 110:1232-1241.
Koyanagi GK, Caraiman D, Blagojevic V, Bohme DK. Gas-Phase Reactions of Transition-Metal Ions with Molecular Oxygen: Room-Temperature Kinetics and Periodicities in Reactivity. 2002. J. Phys. Chem. A 106:4581-4590.
Koyanagi GK, Cheng P, Bohme DK. Gas-phase reactions of atomic lanthanide cations with ammonia: room-temperature kinetics and periodicity in reactivity. 2010. J. Phys. Chem. A 114:241-246.
Koyanagi GK, Zhao X, Blagojevic V, Jarvis MJY, Bohme DK. Gas-phase reactions of atomic lanthanide cations with methyl fluoride: Periodicities in reactivity. 2005. Int. J. Mass Spectrom. 241:189.
Kramida A, Ralchenko Y, Reader J, Team NA. 2012. NIST Atomic Spectra Database (ver. 5.7.1), [Online]. Available: http://physics.nist.gov/asd. National Institute of Standards and Technology, Gaithersburg, MD.
Kretzschmar I, Fiedler A, Harvey JN, Schröder D, Schwarz H. Effects of Sequential Ligation of Molybdenum Cation by Chalcogenides on Electronic Structure and Gas-Phase Reactivity. 1997. J. Phys Chem. A 101:6252-6264.
Kretzschmar I, Schröder D, Schwarz H, Armentrout PB. 2001. The Binding in Neutral and Cationic 3d and 4d Transition-Metal Monoxides and -sulfides. In: Duncan MA, Editor Advances in Metal and Semiconductor Clusters. p 347-394.
Langevin P. Une Formule Fondamentale de Theorie Cinetique. 1905. Ann. Chim. Phys. Ser. 8 5:245-288.
Lavrov VV, Blagojevic V, Koyanagi GK, Orlova G, Bohme DK. Gas-Phase Oxidation and Nitration of First-, Second-, and Third-Row Atomic Cations in Reactions with Nitrous Oxide: Periodicities in Reactivity. 2004. J. Phys. Chem. A 108:5610-5624.
Li F-X, Armentrout PB. Activation of Methane by Gold Cations: Guided Ion Beam and Theoretical Studies. 2006. J. Chem. Phys. 125:133114
Li F-X, Gorham K, Armentrout PB. Oxidation of Atomic Gold Ions: Thermochemistry for the Activation of O_2 and N_2O by Au^+ ($^1S_0$ and ^3D). 2010. J. Phys. Chem. A 114:11043–11052
Li F-X, Hinton CS, Citir M, Liu F-Y, Armentrout PB. Guided Ion Beam and Theoretical Study of the Reactions of Au^+ with H_2, D_2, and HD. 2011. J. Chem. Phys. 134:024310.
Li F-X, Zhang X-G, Armentrout PB. Guided Ion Beam and Theoretical Study of the Reactions of

Ir^+ with H_2, D_2, and HD. 2005. J. Phys. Chem. A 109:8350-8357.
Lindinger W, Alge E, Störi H, Pahl M, Varney RN. Flow-drift tube investigation of some Ar^{++} reactions. 1977. J. Chem. Phys. 67:3495-3499.
Lo HH, Fite WL. Associative Ionization of Ti, Zr, Mg and Th in Collisions with O and O_2. 1974. Chem. Phys. Lett. 29:39-41.
Loh SK, Fisher ER, Lian L, Schultz RH, Armentrout PB. State Specific Reactions of $Fe^+(^6D, ^4F)$ with O_2 and cyclo-C_2H_4O: $D^o_0(Fe^+\text{-}O)$ and Effects of Collisional Relaxation. 1989. J. Phys. Chem 93:3159-3167.
Loh SK, Hales DA, Lian L, Armentrout PB. Collision-Induced Dissociation of Fe_n^+ (n = 2 - 10) with Xe: Ionic and Neutral Iron Cluster Binding Energies. 1989. J. Chem. Phys. 90:5466-5485.
Mulliken RS. Report on Notation for the Spectra of Polyatomic Molecules. 1955. J. Chem. Phys. 23:1997-2011.
Muntean F, Armentrout PB. Guided Ion Beam Study of Collision-Induced Dissociation Dynamics: Integral and Differential Cross Sections. 2001. J. Chem. Phys. 115:1213-1228.
Ng C-Y, Xu Y, Chang Y-C, Wannenmacher A, Parziale M, Armentrout PB. Quantum electronic control on chemical activation of methane by collision with spin–orbit state selected vanadium cation. 2021. Phys. Chem. Chem. Phys. 23:273-286.
Ohanessian G, Brusich MJ, Goddard WA. Theoretical study of transition-metal hydrides. 5. Hafnium to mercury (HfH+ through HgH+), barium and lanthanum (BaH+ and LaH+). 1990. J. Am. Chem. Soc. 112:7179-7189.
Pedley JB, Marshall EM. Thermochemical Data for Gaseous Monoxides. 1983. J. Phys. Chem. Ref. Data 12:967-1031.
Retterer J, Groves KM, Pedersen TR, Caton RG. The electrodynamic effects of MOSC-like plasma clouds. 2017. Radio Science 52:604-615.
Rodgers MT, Walker B, Armentrout PB. Reactions of $Cu^+(^1S$ and $^3D)$ with O_2, CO, CO_2, NO, N_2O, and NO_2 Studied by Guided Ion Beam Mass Spectrometry. 1999. Int. J. Mass Spectrom. 182-183:99-120.
Rue C, Armentrout PB, Kretzschmar I, Schröder D, Harvey JN, Schwarz H. Kinetic-energy Dependence of Competitive Spin-allowed and Spin-forbidden Reactions: $V^+ + CS_2$. 1999. J. Chem. Phys. 110:7858-7870.
Ruscic B, Bross DH. 2019. Active Thermochemical Tables (ATcT) values based on ver. 1.122g of the Thermochemical Network. Argonne National Laboratory.
Santos M, Marçalo J, Matos APd, Gibson JK, Haire RG. Gas-Phase Oxidation Reactions of Neptunium and Plutonium Ions Investigated via Fourier Transform Ion Cyclotron Resonance Mass Spectrometry. 2002. J. Phys. Chem. A 106:7190-7194.
Schröder D, Schwarz H, Clemmer DE, Chen Y, Armentrout PB, Baranov VI, Bohme DK. Activation of hydrogen and methane by thermalized FeO^+ in the gas phase as studied by multiple mass spectrometric techniques. 1997. Int. J. Mass Spectrom. Ion Process. 161:175-191.
Schröder D, Schwarz H, Shaik S. Characterization, Orbital Description, and Reactivity Patterns of Transition-Metal Oxo Species in the Gas Phase. 2000. Struct. Bonding 97:91-123.
Schultz RH, Armentrout PB. Nonadiabatic Behavior of a Transition Metal System: Exothermic Reactions of $Fe^+(^6D,^4F)$ and Propane. 1987. J. Phys. Chem. 91:4433-4435.
Schultz RH, Elkind JL, Armentrout PB. Electronic Effects in C-H and C-C Bond Activation: State-specific Reactions of $Fe^+(^6D, ^4F)$ with Methane, Ethane and Propane. 1988. J. Am. Chem. Soc. 110:411-423.
Shayesteh A, Lavrov VV, Koyanagi GK, Bohme DK. Reactions of Atomic Cations with

Methane: Gas Phase Room-Temperature Kinetics and Periodicities in Reactivity. 2009. J. Phys. Chem. A 113:5602–5611.
Sievers MR, Armentrout PB. The Potential Energy Surface for Carbon-Dioxide Activation by V^+: A Guided Ion Beam Study. 1995. J. Chem. Phys. 102:754-762.
Sievers MR, Armentrout PB. Gas Phase Activation of Carbon Dioxide by Niobium and Niobium Monoxide Cations. 1998. Int. J. Mass Spectrom. 179-180:103-115.
Sievers MR, Armentrout PB. Reactions of CO and CO_2 with Gas Phase Mo^+, MoO^+, and MoO_2^+. 1998. J. Phys. Chem. A 102:10754-10762.
Sievers MR, Armentrout PB. Oxidation of CO and Reduction of CO_2 by Gas Phase Zr^+, ZrO^+, and ZrO_2^+. 1999. Int. J. Mass Spectrom. 185-187:117-129.
Sievers MR, Armentrout PB. Reactions of Y^+, YO^+ and YO_2^+ with CO and CO_2. 1999. Inorg. Chem. 38:397-402.
Sievers MR, Chen Y-M, Armentrout PB. Metal Oxide and Carbide Thermochemistry of Y^+, Zr^+, Nb^+, and Mo^+. 1996. J. Chem. Phys. 105:6322-6333.
Sievers MR, Chen Y-M, Elkind JL, Armentrout PB. Reactions of Y^+, Zr^+, Nb^+, and Mo^+ with H_2, HD, and D_2. 1996. J. Phys. Chem. 100:54-62.
Sorensen JJ, Tieu E, Morse MD. Bond dissociation energies of lanthanide sulfides and selenides. 2021. J. Chem. Phys. 154:124307.
Stowe GF, Schultz RH, Wight CA, Armentrout PB. Translational and Electronic Energy Dependence of $S^+ + H_2(D_2,HD) \rightarrow SH^+(SD^+) + H(D)$. Spin-Allowed and Spin-Forbidden Pathways. 1990. Int. J. Mass Spectrom. Ion Process. 100:177-195.
Sunderlin LS, Armentrout PB. Methane Activation by Ti^+: Electronic and Translational Energy Dependence. 1988. J. Phys. Chem. 92:1209-1219.
Sunderlin LS, Armentrout PB. Rotational Temperature Dependence of the Reaction of N^+ and C^+ with H_2, HD, and D_2. 1994. J. Chem. Phys. 100:5639-5645.
Teloy E, Gerlich D. Integral Cross Sections for Ion-Molecule Reactions. 1. The Guided Beam Technique. 1974. Chem. Phys. 4:417-427.
van Koppen PAM, Kemper PR, Bowers MT. Electronic State-Selected Reactivity of Transition Metal Ions: Co^+ and Fe^+ with Propane. 1992. J. Am. Chem. Soc. 114:10941-10950.
Voislav Blagojevic EF, Michael J.Y. Jarvis, Gregory K. Koyanagi, Diethard K. Bohme. Gas-phase reactions of nitric oxide with atomic lanthanide cations: Room-temperature kinetics and periodicity in reactivity. 2006. Int. J. Mass Spectrom. 249-250:385-391.
Voislav Blagojevic GKKaDKB. ICP-SIFT/MS Study of Gas-Phase Reactions of Lanthanide Cations with Benzene: Room-Temperature Kinetics and Periodicities in Reactivity. 2015. Int. J. Mass Spectrom. 377:484-489.
Wadt WR. Why UO_2^{2+} is Linear and Isoelectronic ThO_2 is Bent. 1981. J. Am. Chem. Soc. 103:6053-6057.
Wiskerke AE, Stolte S, Loesch HJ, Levine RD. $K+CH_3I \rightarrow KI+CH_3$ revisited: the total reaction cross section and its energy and orientation dependence. A case study of an intermolecular electron transfer. 2000. Phys. Chem. Chem. Phys. 2:757-767.
Zhang X-G, Armentrout PB. Reactions of Pt^+ with H_2, D_2, and HD: Effect of Lanthanide Contraction on Reactivity and Thermochemistry. 2002. J. Chem. Phys. 116:5565-5573.
Zhang X-G, Armentrout PB. Activation of O_2 and CO_2 by PtO^+: The Thermochemistry of PtO_2^+. 2003. J. Phys. Chem. A 107:8915-8922.
Zhang X-G, Armentrout PB. Activation of O_2, CO, and CO_2 by Pt^+: The Thermochemistry of PtO^+. 2003. J. Phys. Chem. A 107:8904-8914.

Zhang X-G, Rue C, Shin S-Y, Armentrout PB. Reactions of Ta^+ and W^+ with H_2, D_2, and HD: Effect of Lanthanide Contraction and Spin-Orbit Interactions on Reactivity and Thermochemistry. 2002. J. Chem. Phys. 116:5574-5583.
Zhang Y, Evans JRG, Yang S. Corrected Values for Boiling Points and Enthalpies of Vaporization of Elements in Handbooks. 2011. J. Chem. Eng. Data 56:328-337.
Zhao X, Koyanagi GK, Bohme DK. Gas-phase reactions of atomic lanthanide cations with methyl chloride — Periodicities in reactivity. 2005. Can. J. Chem. 83:1839-1846.
Zhao X, Koyanagi GK, Bohme DK. Reactions of Methyl Fluoride with Atomic Transition-Metal and Main-Group Cations: Gas-Phase Room-Temperature Kinetics and Periodicities in Reactivity. 2006. J. Phys. Chem. A 110:10607-10618.

Table 1. Metal ligand cation bond energies (eV) for selected lanthanides and 5d transition metals

M^+	Elec. Config.	M^+-H	M^+-C	M^+-O	OM^+-O
La^+	$5d^2$	2.48 (0.09)[a]		*8.78 (0.16)*[b]	
Ce^+	$4f^15d^2$	2.19 (0.09)[c]	*2.72 (1.04)*[d]	*8.82 (0.21)*[e]	
Pr^+	$4f^36s^1$	2.10 (0.03)[f]	2.97 (0.10)[g]	7.62 (0.09)[g]	2.47 (0.11)[g]
Nd^+	$4f^46s^1$	1.99 (0.06)[h]	2.61 (0.30)[i]	7.28 (0.05)[i]	2.12 (0.30)[i]
Sm^+	$4f^66s^1$	2.03 (0.03)[j]	2.16 (0.07)[k]	5.72 (0.07)[k]	1.14 (0.15)[k]
Gd^+	$4f^75d^16s^1$	2.18 (0.07)[l]	3.18 (0.18)[m]	7.69 (0.10)[m]	2.86 (0.08)[n]
Lu^+	$4f^{14}6s^2$	2.11 (0.16)[a]		*5.39 (0.16)*[b]	
Hf^+	$5d^16s^2$	2.11 (0.08)[o]	3.19 (0.03)[p]	6.91 (0.11)[p]	
Ta^+	$5d^36s^1$	2.38 (0.06)[q]	3.79 (0.04)[p]	7.10 (0.12)[p]	6.08 (0.12)[r]
				7.01 (0.12)[r]	
W^+	$5d^46s^1$	2.27 (0.05)[q]	4.76 (0.09)[p]	6.77 (0.07)[p]	5.49 (0.09)[r]
				6.72 (0.10)[r]	
Re^+	$5d^56s^1$	2.29 (0.07)[s]	5.13 (0.12)[t]	4.82 (0.03)[u]	6.05 (0.05)[v]
Os^+	$5d^66s^1$	2.45 (0.10)[w]	6.14 (0.14)[t]	4.96 (0.01)[x]	5.31 (0.07)[y]
Ir^+	$5d^76s^1$	3.12 (0.06)[z]	6.58 (0.12)[t]	4.26 (0.05)[aa]	*4.28*[bb]
Pt^+	$5d^9$	2.81 (0.05)[cc]	5.46 (0.05)[dd]	3.26 (0.07)[dd]	3.06 (0.07)[ee]
Au^+	$5d^{10}$	2.13 (0.11)[ff]	*>3.19 (0.08)*[gg]	1.12 (0.08)[hh]	
Th^+	$6d^27s^1/6d^17s^2$	2.45 (0.07)[ii]	4.82 (0.29)[jj]	8.57 (0.14)[jj]	4.94 (0.06)[kk]

Uncertainties in parentheses. Values not from GIBMS results are in *italics*. [a] (Elkind, Sunderlin & Armentrout, 1989). [b] (Gibson, 2003). [c] (Ghiassee & Armentrout, 2020). [d] (Gingerich, 1969). [e] (Cox et al., 2016) and its Supporting Information. [f] (Ghiassee, Ewigleben & Armentrout, 2020). [g] (Ghiassee, Stevenson & Armentrout, 2021). [h] (Ghiassee & Armentrout, 2021). [i] (Ghiassee, Kim & Armentrout, 2019). [j] (Demireva & Armentrout, 2018). [k] (Cox et al., 2015). [l] (Demireva & Armentrout, 2018). [m] (Demireva, Kim & Armentrout, 2016). [n] (Demireva & Armentrout, 2017). [o] (Hinton & Armentrout, 2010). [p] (Hinton, Li & Armentrout, 2009). [q] (Zhang et al., 2002). [r] (Hinton et al., 2011). [s] (Armentrout & Li, 2004). [t] (Kim, Cox & Armentrout, 2016). [u] (Armentrout, 2013). [v] (Kim, Cox & Armentrout, 2020). [w] (Hinton, Citir & Armentrout, 2011). [x] (Hinton, Citir & Armentrout, 2013). [y] (Kim & Armentrout, 2020). [z] (Li, Zhang & Armentrout, 2005). [aa] (Kim & Armentrout, 2021). [bb] Theory value from (Kim & Armentrout, 2021). [cc](Zhang & Armentrout, 2002). [dd] (Zhang & Armentrout, 2003). [ee] (Zhang & Armentrout, 2003). [ff] (Li et al., 2011). [gg] (Aguirre et al., 2000) as reinterpreted in (Li & Armentrout, 2006). [hh] (Li, Gorham &

Armentrout, 2010). [ii] (Cox, Armentrout & de Jong, 2016). [jj] (Cox et al., 2016). [kk] (Armentrout & Peterson, 2020).

Figure Captions

FIGURE 1. Cross sections for reactions of O_2 with Hf^+ (red triangles), Ta^+ (black circles), W^+ (green inverted triangles)(Hinton, Li & Armentrout, 2009), Re^+ (blue squares)(Armentrout, 2013), Os^+ (pink diamonds)(Hinton, Citir & Armentrout, 2013), Ir^+ (purple triangles)(Armentrout & Li, 2013), Pt^+ (red inverted triangles)(Zhang & Armentrout, 2003), Au^+ (^1S) (yellow circles), and Au^+ (^3D) (yellow triangles)(Li, Gorham & Armentrout, 2010) as measured using GIBMS. The arrow indicates the BDE of O_2 at 5.117 eV. The black line shows the LGS collision cross section. [Color figure can be viewed at wileyonlinelibrary.com].

FIGURE 2. Cross sections for reactions of O_2 with Pr^+ (blue squares)(Ghiassee, Stevenson & Armentrout, 2021), Nd^+ (pink diamonds)(Ghiassee, Kim & Armentrout, 2019), Sm^+ (purple triangles)(Cox et al., 2015), Gd^+ (green inverted triangles)(Demireva, Kim & Armentrout, 2016), and Th^+ (black circles), as measured using GIBMS. The arrow indicates the BDE of O_2 at 5.117 eV. The black line shows the LGS collision cross section. [Color figure can be viewed at wileyonlinelibrary.com].

FIGURE 3. Cross sections for reactions of CO to form MO^+ (part a) and MC^+ (part b) with Hf^+ (red triangles), Ta^+ (black circles), W^+ (green inverted triangles)(Hinton, Li & Armentrout, 2009), Re^+ (blue squares), Os^+ (pink diamonds), Ir^+ (purple triangles)(Kim, Cox & Armentrout, 2016), and Pt^+ (red inverted triangles, with line showing total cross section)(Zhang & Armentrout, 2003) as measured using GIBMS. The arrow indicates the BDE of CO at 11.111 eV. [Color figure can be viewed at wileyonlinelibrary.com].

FIGURE 4. Cross sections for reactions of CO to form MO^+ (part a) and MC^+ (part b) with Pr^+ (blue squares)(Ghiassee, Stevenson & Armentrout, 2021), Nd^+ (pink diamonds)(Ghiassee, Kim & Armentrout, 2019), Sm^+ (purple triangles)(Cox et al., 2015), Gd^+ (green inverted triangles) (Demireva, Kim & Armentrout, 2016), and Th^+ (black circles)(Cox et al., 2016), as measured using

GIBMS. The arrow indicates the BDE of CO at 11.111 eV. [Color figure can be viewed at wileyonlinelibrary.com].

FIGURE 5. Cross sections for reactions of CO_2 to form MO^+ (solid symbols) and MCO^+ (open symbols, x10 except for $PtCO^+$) with Pr^+ (blue squares)(Ghiassee, Stevenson & Armentrout, 2021), Nd^+ (pink diamonds)(Ghiassee, Kim & Armentrout, 2019), Sm^+ (purple triangles) (Armentrout & Cox, 2017), Gd^+ (green inverted triangles)(Demireva & Armentrout, 2018), and Pt^+ (red inverted triangles)(Zhang & Armentrout, 2003), as measured using GIBMS. The arrow indicates the BDE of CO_2 at 5.45 eV. The black dashed line is the LGS collision cross section. The red line is the total cross section for reaction with Pt^+. [Color figure can be viewed at wileyonlinelibrary.com].

FIGURE 6. Part a. Cross sections for reactions of H_2 with Hf^+ (red triangles)(Hinton & Armentrout, 2010), Ta^+ (black circles), W^+ (green inverted triangles)(Zhang et al., 2002), Re^+ (blue squares) (Armentrout & Li, 2004), Os^+ (pink diamonds)(Hinton, Citir & Armentrout, 2011), Ir^+ (purple triangles)(Li, Zhang & Armentrout, 2005), Pt^+ (red inverted triangles)(Zhang & Armentrout, 2002), and Au^+ (yellow circles)(Li et al., 2011) as measured using GIBMS. The arrow indicates the BDE of H_2 at 4.479 eV. Part b. Cross sections for reactions of D_2 with Ce^+ (red triangles)(Ghiassee & Armentrout, 2020), Pr^+ (blue squares)(Ghiassee, Ewigleben & Armentrout, 2020), Nd^+ (pink diamonds)(Ghiassee & Armentrout, 2021), Sm^+ (purple triangles)(Demireva & Armentrout, 2018), Gd^+ (green inverted triangles)(Demireva & Armentrout, 2018), and Th^+ (black circles)(Cox, Armentrout & de Jong, 2016) as measured using GIBMS. The arrow indicates the BDE of D_2 at 4.556 eV. [Color figure can be viewed at wileyonlinelibrary.com].

FIGURE 7. Lanthanide oxide cation bond dissociation energies as a function of the promotion energy to either a $5d^16s^1$ (red triangles) or $5d^2$ (black circles) electron configuration for Ln^+ or the Ln^{2+} ($5d^1$) (blue inverted triangles) electron configuration. Full lines are linear regression fits to all the data. The dashed black line has a slope of -1. BDEs not included in Table 1 and all E_p values for Ln^+ are from (Gibson, 2003) and the IE(Ln^+) and $E_p(Ln^{2+},5d^1)$ values are from (Kramida et al., 2012). [Color figure can be viewed at wileyonlinelibrary.com].

FIGURE 8. Metal ligand cation bond dissociation energies across the periodic table. All values are from Table 1. Vertical lines indicate breaks in the periodic sequence. The horizontal red dashed line indicates $D_0(O_2)$. [Color figure can be viewed at wileyonlinelibrary.com].

FIGURE 9. Molecular orbitals calculated for linear $OThO^+$. Adapted from (Armentrout & Peterson, 2020). [Color figure can be viewed at wileyonlinelibrary.com].

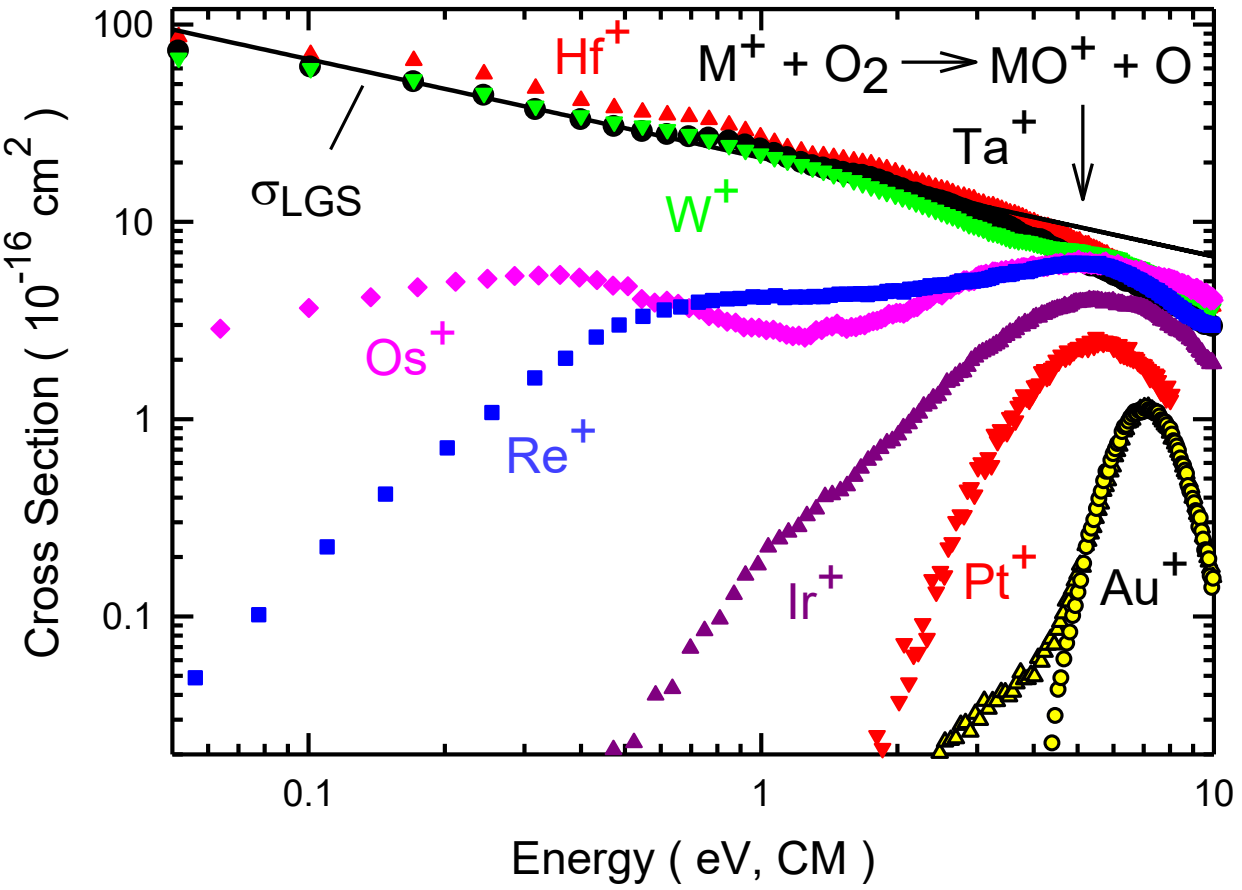
100
10
1
0.1
0.1
1
10
Cross Section (10-16 cm2)
Energy (eV, CM)
Hf+
M+ + O2 → MO+ + O
Ta+
σLGS
W+
Os+
Re+
Ir+
Pt+
Au+

Figure 1

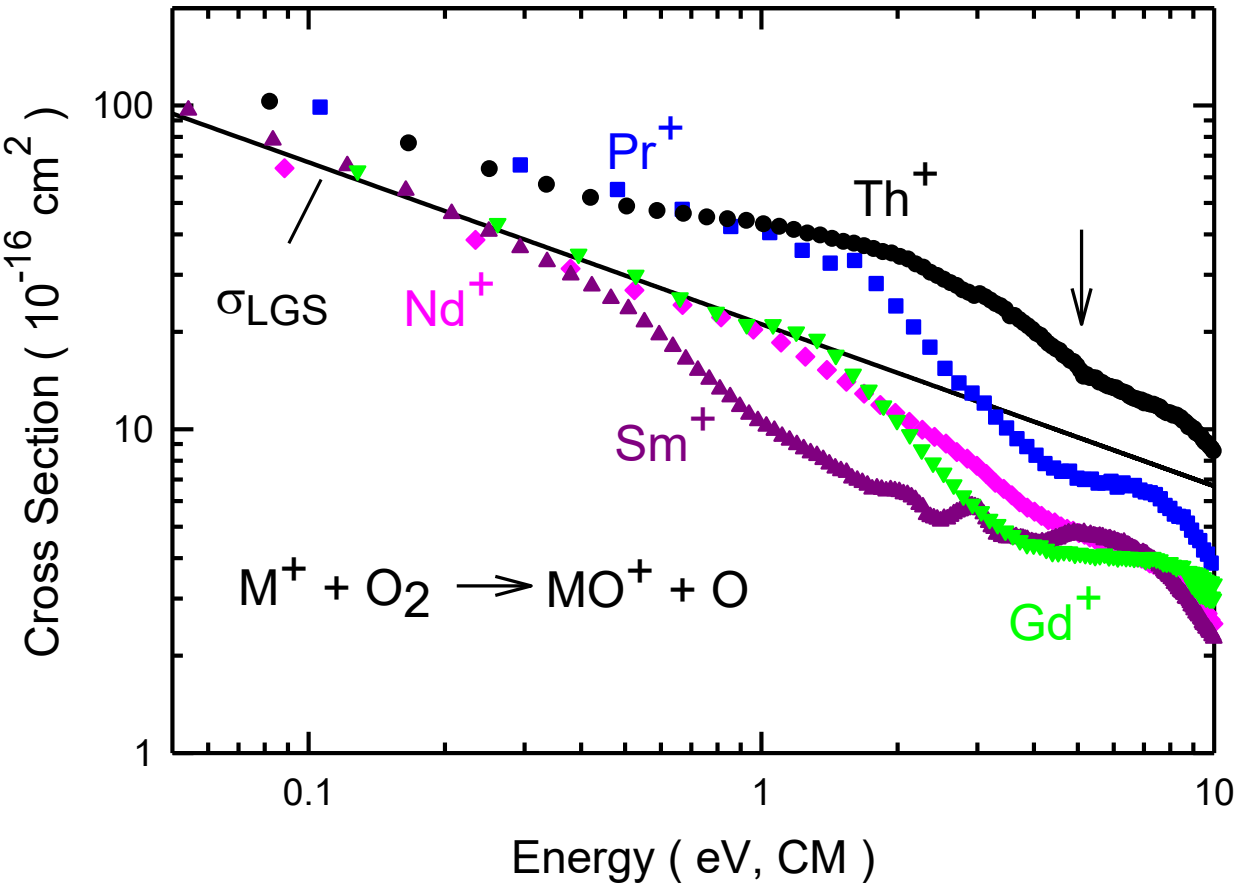
Cross Section (10-16 cm2)
100
10
1
0.1
1
10
Energy (eV, CM)
σLGS
Pr+
Th+
Nd+
Sm+
Gd+
M+ + O2 → MO+ + O

Figure 2

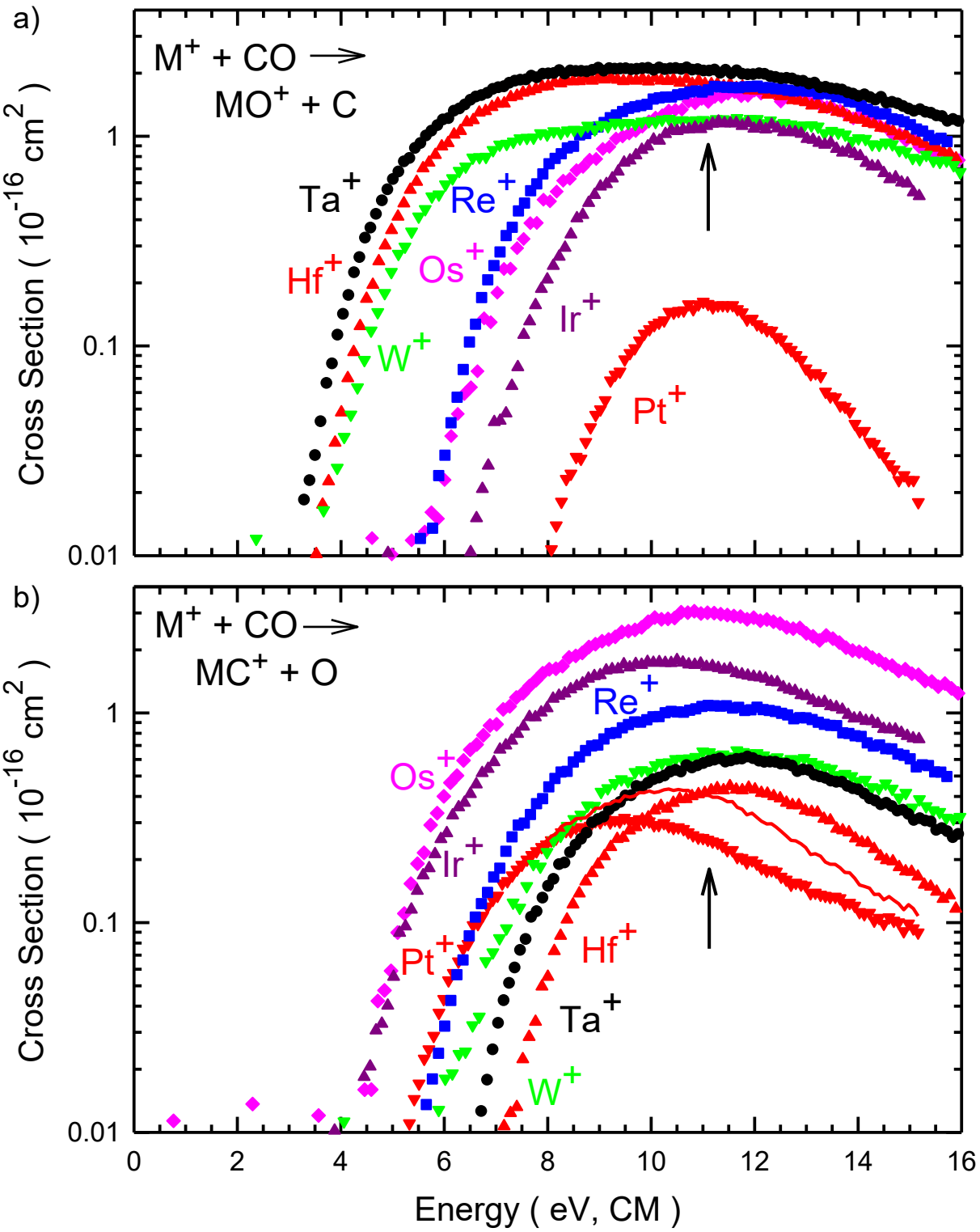
a)
M+ + CO →
MO+ + C
Ta+
Re+
Hf+
Os+
Ir+
W+
Pt+
Cross Section (10-16 cm2)
1
0.1
0.01
b)
M+ + CO →
MC+ + O
Re+
Os+
Ir+
Pt+
Hf+
Ta+
W+
Cross Section (10-16 cm2)
1
0.1
0.01
0
2
4
6
8
10
12
14
16
Energy (eV, CM)

Figure 3

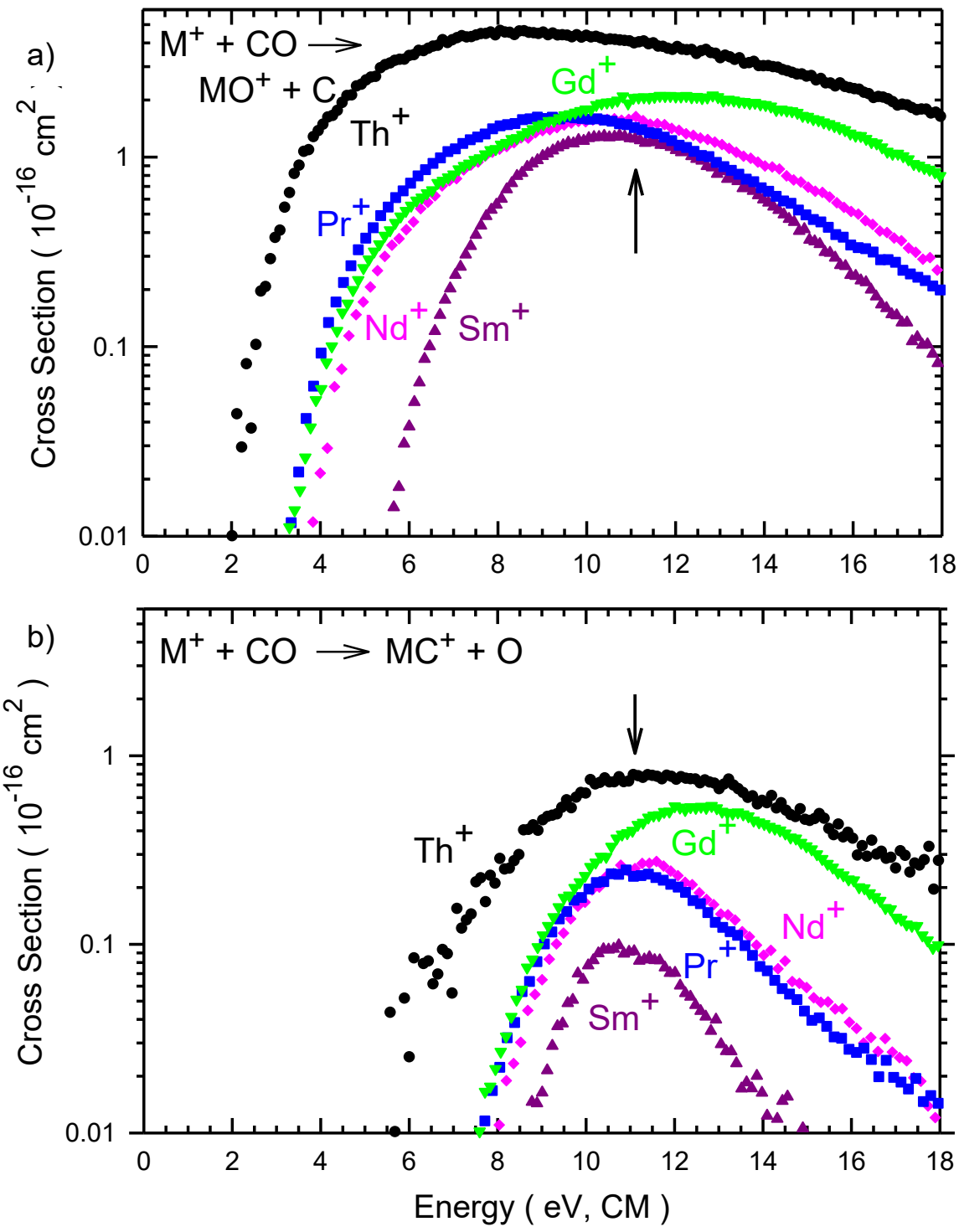
a)
M+ + CO →
MO+ + C
Th+
Gd+
Pr+
Nd+
Sm+
Cross Section (10-16 cm2)
0.01
0.1
1
0
2
4
6
8
10
12
14
16
18
b)
M+ + CO → MC+ + O
Th+
Gd+
Nd+
Pr+
Sm+
Cross Section (10-16 cm2)
0.01
0.1
1
0
2
4
6
8
10
12
14
16
18
Energy (eV, CM)

Figure 4

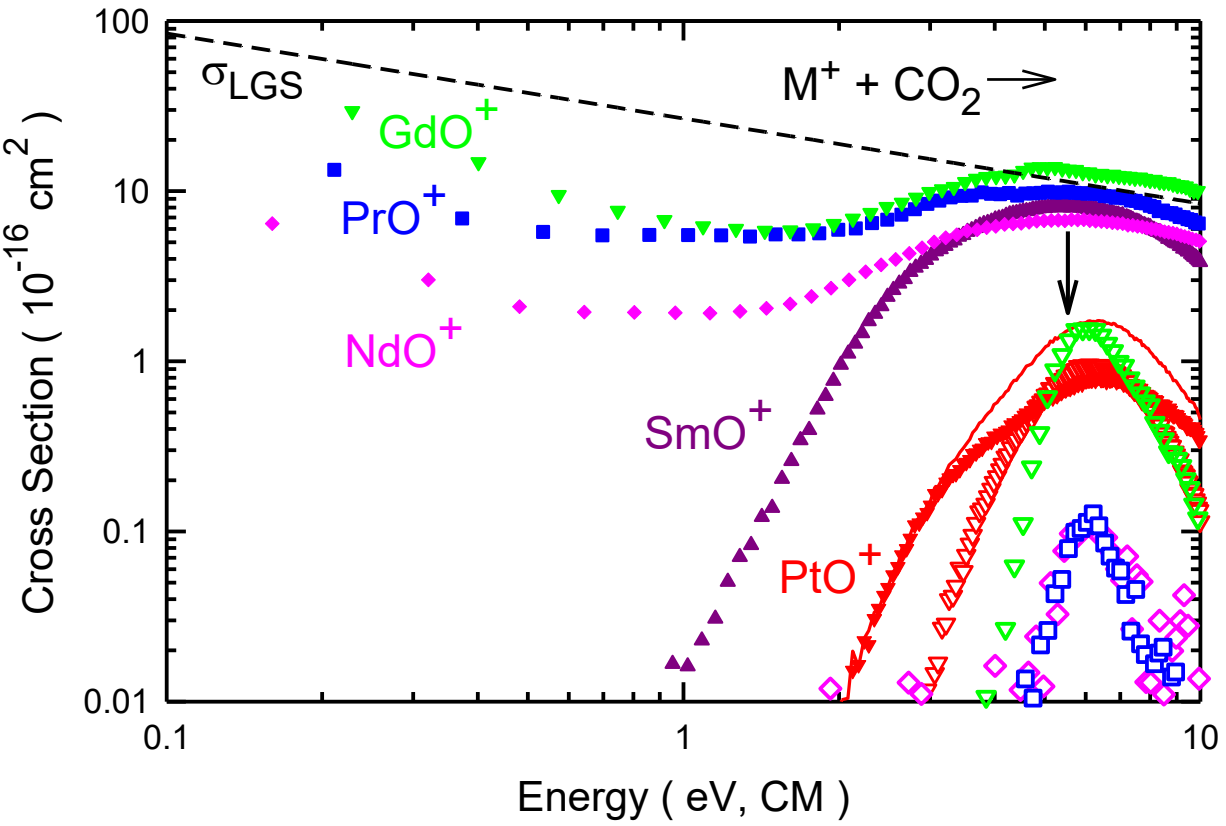
100
10
1
0.1
0.01
0.1
1
10
Cross Section (10-16 cm2)
Energy (eV, CM)
σLGS
M+ + CO2
GdO+
PrO+
NdO+
SmO+
PtO+

Figure 5

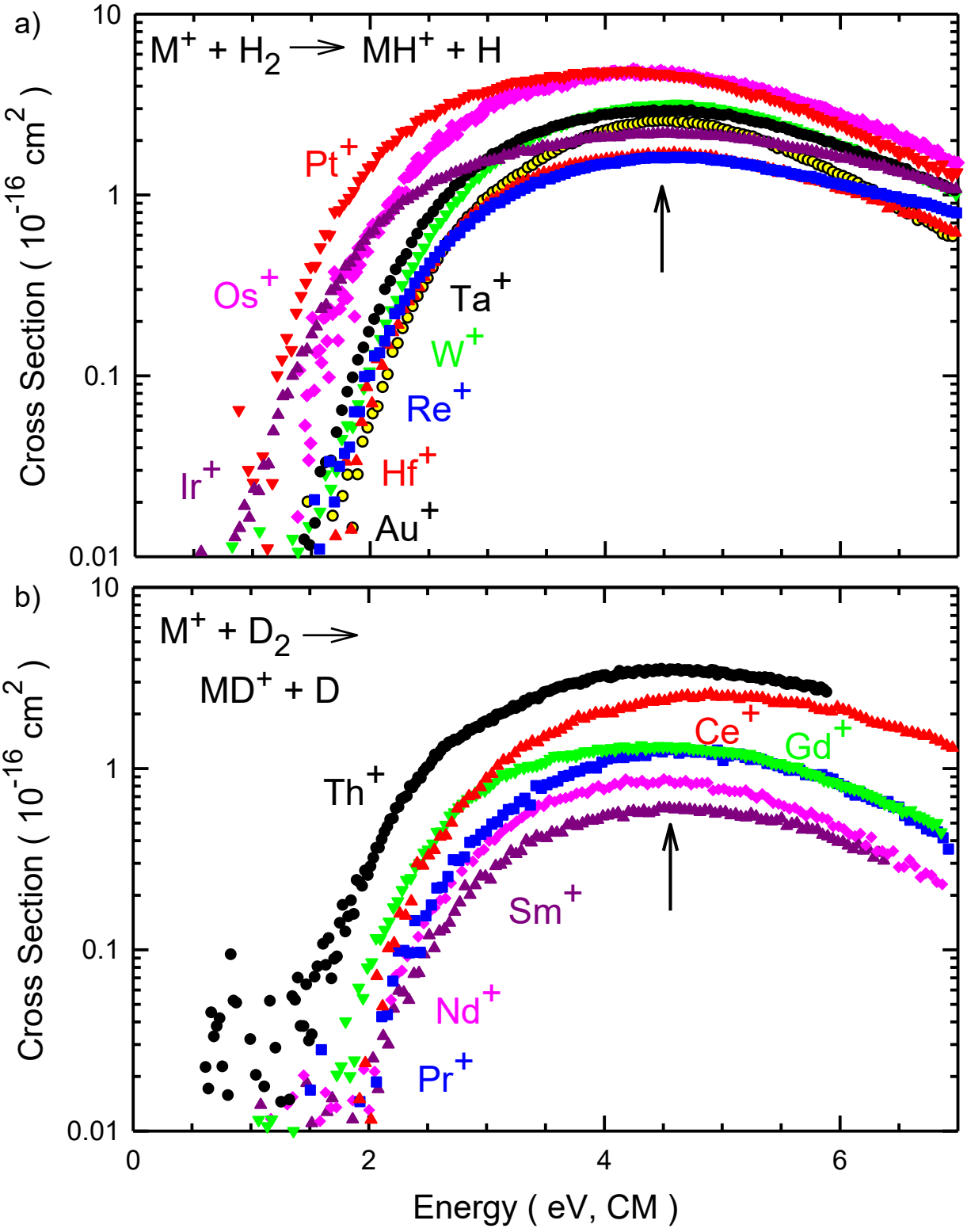
a)
M+ + H2 → MH+ + H
Pt+
Os+
Ta+
W+
Re+
Ir+
Hf+
Au+
Cross Section (10-16 cm2)
10
1
0.1
0.01
b)
M+ + D2 →
MD+ + D
Th+
Ce+
Gd+
Sm+
Nd+
Pr+
Cross Section (10-16 cm2)
10
1
0.1
0.01
0
2
4
6
Energy (eV, CM)

Figure 6

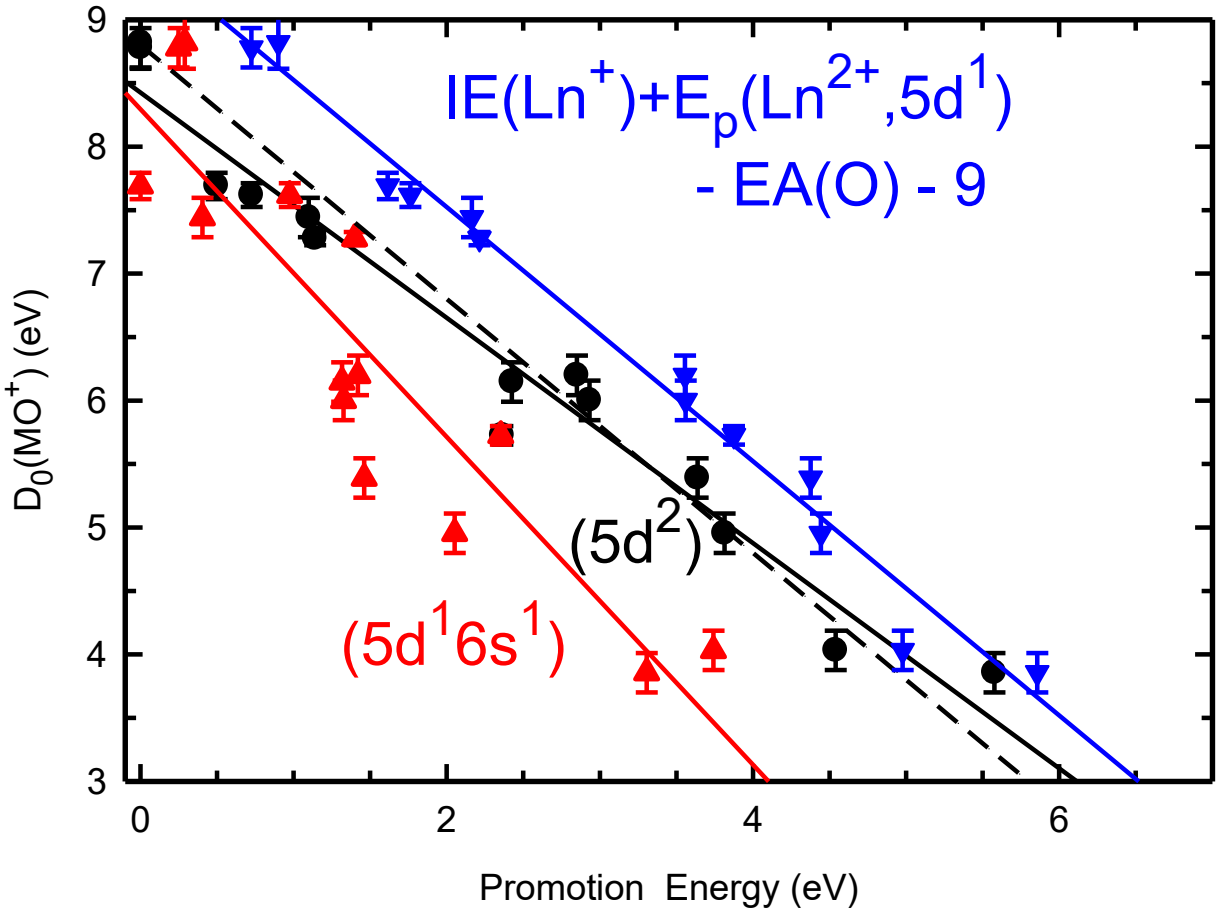
IE(Ln+)+Ep(Ln2+,5d1)
- EA(O) - 9
(5d2)
(5d16s1)
D0(MO+) (eV)
Promotion Energy (eV)
9
8
7
6
5
4
3
0
2
4
6

Figure 7

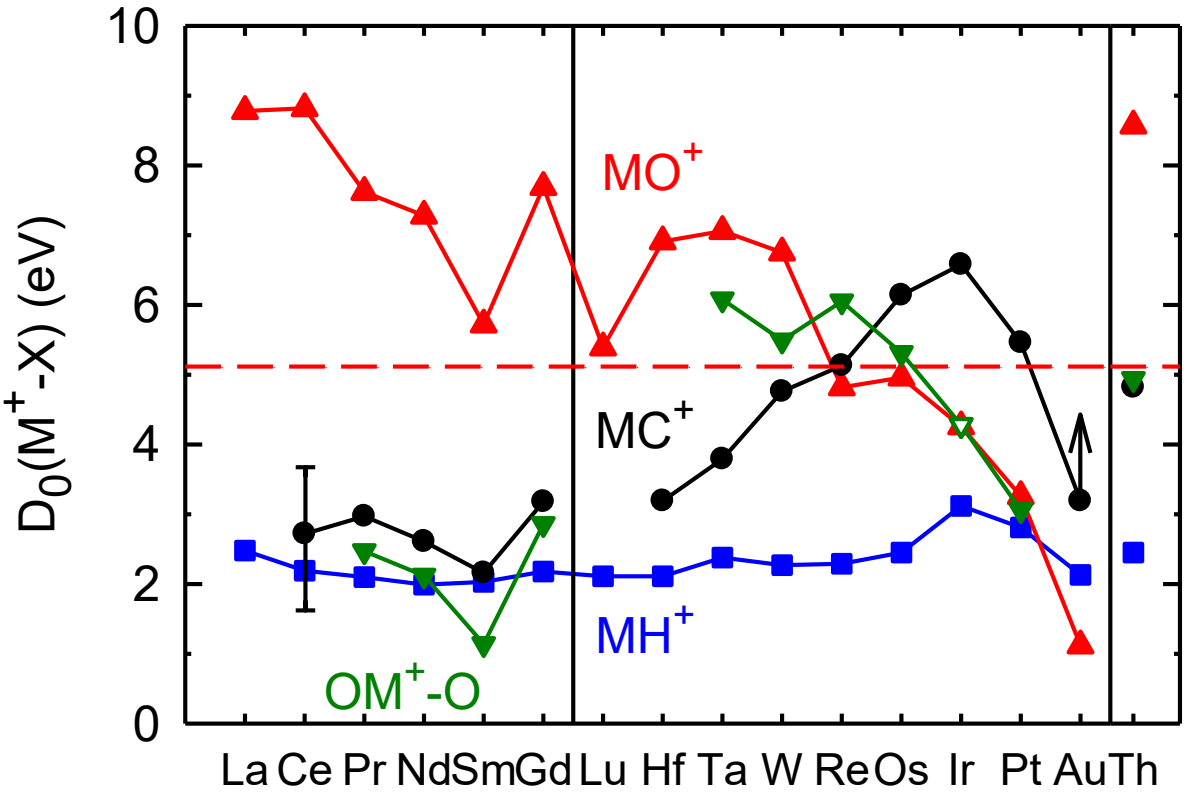

Figure 8

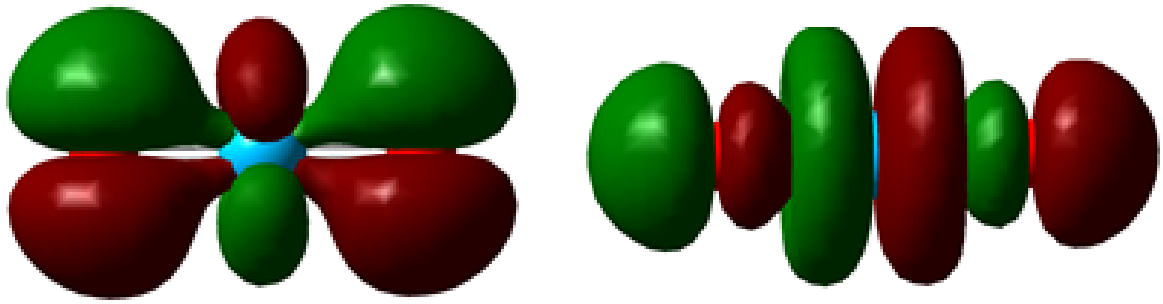

Figure 9